Ocean Wavenumber Estimation From Wave-Resolving Time Series Imagery

Nathaniel G. Plant, K. Todd Holland, and Merrick C. Haller

***Abstract*—We review several approaches that have been used to estimate ocean surface gravity wavenumbers from wave-resolving remotely sensed image sequences. Two fundamentally different approaches that utilize these data exist. A power spectral density approach identifies wavenumbers where image intensity variance is maximized. Alternatively, a cross-spectral correlation approach identifies wavenumbers where intensity coherence is maximized. We develop a solution to the latter approach based on a tomographic analysis that utilizes a nonlinear inverse method. The solution is tolerant to noise and other forms of sampling deficiency and can be applied to arbitrary sampling patterns, as well as to full-frame imagery. The solution includes error predictions that can be used for data retrieval quality control and for evaluating sample designs. A quantitative analysis of the intrinsic resolution of the method indicates that the cross-spectral correlation fitting improves resolution by a factor of about ten times as compared to the power spectral density fitting approach. The resolution analysis also provides a rule of thumb for nearshore bathymetry retrievals—short-scale cross-shore patterns may be resolved if they are about ten times longer than the average water depth over the pattern. This guidance can be applied to sample design to constrain both the sensor array (image resolution) and the analysis array (tomographic resolution).**

***Index Terms*—Adaptive signal processing, image processing, sea floor, sea surface, wavelength measurement.**

I. Introduction

INCREASINGLY, observations of coastal processes are required over wide areas and at high spatial and temporal resolutions. In particular, recent modeling advances enable the simulation of wave parameters and wave-driven flows at resolutions as fine as a few meters. These model predictions require initial and boundary conditions, and because model results are often very sensitive to the details of the water depths, the bathymetry is an important boundary condition. In addition, the bathymetry may evolve significantly in several hours during storms or over longer time periods under more quiescent conditions. Therefore, providing models with up-to-date bathymetry is required to achieve accurate predictions. Furthermore, continuous bathymetric observations are essential in understanding the overall sediment and morphologic dynamics in coastal regions. As these observations are required both over large spatial regions and continuously in time, direct surveying methods are not up to this challenge, and remote sensing methods are required.

Shore-based remote sensing platforms can provide a continuous data stream that is also synoptic, typically spanning the region from the shoreline out to intermediate depths. For example, video camera stations are a numerous and well-established data source [1], [2]. With these data, it is possible to see the kinematic interaction of the incident wave field with the bathymetry (i.e., wave shoaling and refraction); hence, this information can be used to obtain estimates of bathymetry [3], [4]. An alternative approach for estimating bathymetry that utilizes time-averaged estimates of dissipation from remote sensing data [5]–[7] can only be applied in the surf zone and at the shoreline [8], [9]. It is possible to estimate bathymetry using other remote sensing approaches, such as multispectral or hyperspectral analysis [10], [11], which are typically deployed from aircraft.

Approaches to bathymetry estimation that are based on wave kinematics utilize the depth dependence of the wave speed or, equivalently, the wavelength and frequency, since $c = f/k$, where c is the wave phase speed, f is the wave frequency, and k is the wavenumber $= 1/L$, in which L is the wavelength. Overall, this approach requires image sequences, or time series of intensity at discretely sampled locations, that adequately resolve the wave motions. This situation differs from typical applications that use airborne or space-borne platforms, as those systems do not have long-enough dwell time to temporally resolve the surface waves but may be able to resolve the slowly varying current field [12].

The underlying methodology to solve this surface wave kinematics estimation problem has taken a number of different forms. These include finding the frequency and wavenumbers where spectral energy is a maximum [13]–[15], estimating the wavelength directly from a cross-shore-oriented pixel array at particular frequencies [3], estimating the time delay between a pair of image locations [16], and estimating spatial translations of the image field (the so-called particle image velocimetry) from sequential image pairs [17]. Once the wave speeds (or wavelengths) have been estimated, the data can be used to estimate depth via a wave dispersion relationship. This last step requires an inverse model solution that solves for a depth AQ2
that minimizes differences between the predicted speed (from the dispersion relationship) and the estimated speed (from the imagery).

The diverse methodologies listed above are similar in that most are designed to extract estimates of wavenumber

Manuscript received January 25, 2008; revised xxxx. This work was supported by the Office of Naval Research through the base funding program element under Contract 0602435N. AQ1

N. G. Plant was with the Naval Research Laboratory, Stennis Space Center, MS 39529 USA. He is now with the U.S. Geological Survey, Florida Integrated Science Center, St. Petersburg, FL 33701 USA (e-mail: nplant@usgs.gov).

K. T. Holland is with the Naval Research Laboratory, Stennis Space Center, MS 39529 USA (e-mail: tholland@nrlssc.navy.mil).

M. C. Haller is with the School of Civil and Construction Engineering, Corvallis, OR 97331 USA (e-mail: hallerm@engr.orst.edu).

Color versions of one or more of the figures in this paper are available online at http://ieeexplore.ieee.org.

Digital Object Identifier 10.1109/TGRS.2008.919821

components at discrete frequencies from the imagery. However, it is not clear how well each method performs in a wide range of environments, including the laboratory, open water (where wavenumber variations that are controlled by currents may be important), open coasts (i.e., long straight beaches), and enclosed coasts (which have inlets and strong wave–current interactions). In addition, it is not clear how well each method can be applied to other imaging modalities, such as microwave radar [18], [19]. Therefore, the objective of this paper is to quantify the sensitivity of wavenumber estimation methods to variations in the sample design (e.g., spatial and temporal resolutions) and signal-to-noise ratios of the imaging system. To understand the situation, we will decouple the wavenumber estimation problem from that of estimating water depth. To this end, we define the problem, and we derive a formal inverse model that solves for the unknown spatially variable wavenumbers from image sequences (or intensity time series from a subset of image pixels). We evaluate the suitability of various sampling scenarios, including 1- and 2-D spatial arrays. In addition, we evaluate the abilityto predict the errors of the wavenumber estimates. Error predictions are essential for quantitative quality control and impact the results of subsequent bathymetry estimations as well as field evaluations of, for example, wave dispersion models [4], [20].

This paper is organized as follows. In Section II, we describe the general problem of wave phase speed estimation and its equivalent wavenumber estimation problem, and we derive an inverse model for estimating spatially varying wavenumbers. In Section III, we evaluate the skill of the newly developed method using both synthetic and real-world data sets applied to both 1- and 2-D spatial domains. In Section IV, we discuss the similarity and differences between existing wavenumber estimation approaches, and we quantify the theoretical constraints on the spatial resolution of wavenumber and bathymetry estimates. Section V summarizes the important results, including the following: 1) that the proposed method provides improved spatial resolution and quantitative error predictions and 2) that it is well suited to solve the bathymetry inversion problem.

II. Theory

We assume that georeferenced image sequences exhibiting intensity modulations attributable to surface gravity waves are available and that their sampling rate is sufficient to resolve a significant portion of the gravity wave spectrum. The imagery can be expressed as $I(x_i, y_i, t)$, where x_i, y_i is the spatial coordinate of the ith image pixel, and t represents discrete sampling times. At frequencies of interest, we wish to characterize the spatial variation of the wave field, including the changes in wavelength and direction that occur in nearshore areas due to shoaling and refraction.

Our first objective is to describe an efficient and accurate method of calculating estimates of c (or, equivalently, k). We will make some additional simplifying assumptions. For example, many details regarding the sensor imaging mechanisms, such as light absorption, reflection, and scattering, are ignored [21]. Variance introduced at sum/difference frequencies and wavenumbers via wave nonlinearity is also ignored [22]. The (spatially) unresolved portion of the image signal, corresponding to water waves that are shorter than the Nyquist wavelength of the image samples, is not treated in detail other than to assume that it will appear as white noise. This aliased component can be resolved [15], [23], but this is probably only required if we were attempting to reconstruct the details of the time-varying sea surface. Instead, our focus is on extracting the resolvable spatial variability of the wavenumber vector field. Finally, we assume that this variability can be described by a finite number of modes. For example, a particularly egregious assumption will be that the wave field at a single frequency is locally well represented by a single wavelength and direction. Our approach tests this particular hypothesis with a quantitative model so that violations can be identified.

A. *Time Delay Problem Definition*

We assume that time delay information is available from the spatially separated pixels such that an intensity time series at one location can be predicted from observations at another location, i.e.,

$$I(x_i, y_i, t) = g_{i,j,n} I(x_j, y_j, t + \Delta t_{i,j,n}) + e_{i,j,n}(t) \qquad \text{(1a)}$$

where the time lag $\Delta t_{i,j,n}$ maximizes the correlation or minimizes the variance of the error $e_{i,j,n}$ between observations at sample locations x_i, y_i and x_j, y_j due to the nth wave component. The parameter $g_{i,j,n}$ is a tunable correlation coefficient. In one spatial dimension (e.g., normal to the shoreline), the time lag is related to the wave properties as

$$\begin{aligned}\Delta t_{i,j,n} &= \int_{x_i}^{x_j} \frac{\cos(\alpha_n[x])}{c_n[x]} dx \\ &= \int_{x_i}^{x_j} \frac{\cos(\alpha_n[x])\, k_n[x]}{f_n} dx \qquad \text{(1b)}\end{aligned}$$

where α_n is the direction of the nth wave component (e.g., it corresponds to a discrete frequency and wavenumber f_n, k_n, respectively), and c_n is the celerity of that wave component. The cosine inside the integral indicates that the analysis only resolves the wave component in the shore-normal direction. This equation is the basis for any tomographic analysis applied to physical properties of the Earth [24], including the speed of sound waves in the ocean [25].

The wave field can be described in a discrete spatial domain with spacing Δx. The discrete time delay equation becomes

$$\begin{aligned}\Delta t_{i,j,n} &= \Delta x \sum_{m=1}^{M} D_{i,j,m} \frac{\cos(\alpha_n[x_m])}{c_n[x_m]} \\ &= \Delta x \sum_{m=1}^{M} D_{i,j,m} \frac{\cos(\alpha_n[x_m])}{f_n} k_n[x_m] \qquad \text{(2)}\end{aligned}$$

where the matrix D is a design matrix defined on both the sample domain x_i, x_j and the estimation domain described by location x_m. (We will refer to the estimation domain as the tomographic domain to maintain that analogy.) The design matrix describes how each observation contributes information to the estimate of the unknown model parameters $\alpha_{n,m}$ and $k_{n,m}$. In 1-D, elements of D are equal to unity between two sensors and are zero elsewhere. Smoothness constraints can be implemented through filtering of D such that sharp changes in the estimated celerity are not permitted.

Clearly, in this form, the time delay equation is linear with respect to the unknown wavenumbers. The number of observations required to solve the problem must be at least equal to the number of elements M in the tomographic domain. Furthermore, the spatial distribution of the observations is important. For instance, an element in the center of an array of observations will have many contributions, whereas elements at the ends of the array will have fewer contributions. Thus, while the resolution of x_m is arbitrary, the resolvable scales of intensity variance depend on the data sampling resolution.

To utilize the time delay equation with remotely sensed imagery, one must estimate the time lag Δt associated with the propagation of the visible wave signal. The time lag will differ for all sensor pairs. This requires some sort of a search for the Δt that corresponds to a maximum in the cross correlation function $r_{i,j}$, as given by

$$r_{i,j}(\Delta t) = W(\Delta t)^* \left\langle I(x_i, t) I(x_j, t + \Delta t)\right\rangle \tag{3}$$

where W is a bandpassed filter that is convolved against the cross correlation, and the angle brackets indicate an ensemble average over all observation times. This method has recently been used, for instance, in the estimation of flow speeds with fiber optic sensors [26]. At this stage, the estimation of the time delays typically requires a nonlinear search algorithm; therefore, the linearized version of the time delay equation does not avoid a nonlinear estimation step.

B. Phase Delay Problem Definition

Since it is natural to work with wave processes in the frequency domain, an alternative approach is to apply a discrete Fourier transform to the observations and rewrite the time delay as a phase delay by computing the cross-spectral correlation between two sensors as follows:

$$\begin{aligned} C_{i,j,f}^{\mathrm{OBS}} &= \left\langle \tilde{I}(x_i, f)\tilde{I}^*(x_j, f)\right\rangle \\ &= \gamma_{i,j,f}\exp\{\sqrt{-1}\Phi_{i,j,f}\} \end{aligned} \tag{4}$$

where the tilde indicates the Fourier transform, the asterisk indicates the complex conjugate, angle brackets indicate ensemble or band averaging, γ is the coherence, and Φ is the phase shift between two sample locations x_i and x_j for a particular frequency. Since the phase shift between two sensors is $\Phi_{i,j,f} = f\Delta t_{i,j,f}$, replace Δt with the right-hand side of (2), and insert the resulting expression for Φ into (4) to get a model for the cross-spectral correlation, which is described as follows:

$$C_{i,j,f}^{\mathrm{MODEL}} = \exp\left\{2\pi\Delta x\sqrt{-1}\sum_{m=1}^{M} D_{i,j,m}k_{m,f}\cos(\alpha_{m,f})\right\}. \tag{5}$$

While the time delay equation is linear in the cross-shore wavenumber $k_{m,f}\cos(\alpha_{m,f})$, the cross-spectral correlation equation is a nonlinear function of the wavenumber.

An apparent advantage of the spectral formulation is that the problem of filtering the time series within particular frequency bands is accomplished via Fourier transform, and the nonlinear problem of identifying time delays in the observations is avoided. A disadvantage of the Fourier transform approach is a requirement for sufficient sample duration to resolve the frequencies of interest. This disadvantage is mitigated by the use of coherence to identify robustness of the analysis. A further disadvantage is that a phase ambiguity exists such that $\Phi_{\mathrm{estimate}} = \Phi_{\mathrm{true}} - (2\pi b)$, where b is the phase ambiguity, and Φ_{estimate} lies on the interval $(-\pi, \pi)$. Thus, sample locations that are separated by more than a wavelength are susceptible to aliasing when the phase ambiguity is unknown. (Piotrowski and Dugan [15] deal with this by guessing at the ambiguities.) This problem is well known and has received much recent attention in applications of synthetic aperture radar interferometry. The solutions for cases with potentially large phase ambiguities may be solved via simulated annealing [27]. In the present approach, we will assume that there are a sufficient number of sensor separations that suffer no phase ambiguity—given a decent initial guess of the true wavenumbers, these sensor separations can be identified *a priori*. A data-adaptive identification method is explained in Section II-C-3.

C. Wavenumber Estimation Solution Methods

Previous approaches to estimating wavenumbers (and directions) at a particular frequency contain different mixtures of local and nonlocal solutions to the problem. For instance, the approach of Piotrowski and Dugan [15] assumes locally horizontal bathymetry (implying spatially constant wavenumber magnitude and wave direction over an analysis region) and calculates the image intensity spectrum as a function of two wavenumber components and frequency via Fourier transforms. This spatially homogeneous spectrum assumption is applied over a large number of nearby sample locations (commonly a 256×256 patch of pixels, with a typical resolution of 1 $\mathrm{m}^2\mathrm{pixel}^{-1}$). For all wavenumber components, a frequency of maximum spectral density is identified. This approach does not directly utilize correlations across regions where the wavenumber is changing (in the shoaling region), which are explicitly contained in the formulation given by (2). There are other approaches used to analyze spectral energy distribution of wavenumber (e.g., [28] and [29]), but these also assume spatial homogeneity.

We seek to avoid the restriction of spatial homogeneity because, for example, it is commonly not applicable in nearshore areas where bathymetry and currents can induce rapid wavenumber variations over short distances and where a higher resolution is required. Hence, we turn our attention to solution methods that fully utilize the available spatial correlation information. These allow a highly resolved spatially variable wavenumber field. Furthermore, we will focus on the spectral approach based on (4) rather than the time-domain approach that would be based on (2).

1) Single-Mode Analysis: In general, at a single frequency, numerous wave trains, each with different directions, could contribute to the cross-spectral correlation estimate defined by (4). Thus, the original tomographic equation relating time delay to wave speed is inherently a stochastic problem, with each wave train contributing to and blurring the best-fit speeds and the corresponding time delays. One possible approach for separation of the various contributing wave trains is to decompose the cross-spectral correlation into the most coherent modes as follows:

$$C^{\mathrm{OBS}}_{i,j,f} = \sum_{q=1}^{Q} P_{i,q,f}\Gamma_{q,f}P^{*}_{j,q,f} \tag{6}$$

where $\Gamma_{q,f}$ is the $Q \times Q$ diagonal matrix with eigenvalues of $C^{\mathrm{OBS}}_{i,j,f}$, and $P_{i,q,f}$ are the corresponding eigenvectors. In their approach to estimating bathymetry from video imagery this way, Stockdon and Holman [3] selected the first (dominant) eigenmode to approximate the cross-spectral matrix at a single dominant frequency. The magnitude of the eigenvector at each location x_i indicates its contribution to the total correlation, and the spatial phase differences are described by the phase of the eigenvector. To extract wavenumber information, which is related to the gradient of the phase, Stockdon and Holman [3] unwrapped the phases of P and estimated the local gradient of the potentially noisy phase estimates, e.g.,

$$\hat{k}_{i,f} = \frac{1}{2\pi}\frac{\hat{\phi}_{i+1,1,f} - \hat{\phi}_{i-1,1,f}}{(x_{i+1} - x_{i-1})}. \tag{7}$$

This estimate is the cross-shore component of the dominant wavenumber, and the full wavenumber requires an estimate of the alongshore component, which they obtained from a different analysis approach and was assumed constant across the domain.

Although this method is computationally efficient, it suffers several disadvantages. First, using only the first eigenmode requires significant coherence across the entire domain. Typically, the center of the domain will dominate the first mode [30]. Thus, the phase estimates at the offshore and onshore ends of the array and at the location of wave breaking (where coherence and phase are disrupted by changes in the imaging mechanism for optical data) may be poorly estimated. Second, phase errors due to observation noise or phase ambiguity are difficult to estimate, which is problematic because error predictions are essential for assessing the value of the extracted data. A potentially devastating situation is that of an array with very dense samples such that the denominator of (7) approaches zero and the estimate primarily amplifies measurement errors, rather than identifying the slowly varying wavenumber. Finally, there is potentially useful information at multiple wave frequencies in addition to that at the "dominant" frequency. The identification of a "dominant" frequency involves tradeoffs between signal strength, spatial coherence, and spatial resolution. These attributes are not necessarily the maximum at all spatial locations at the "dominant" frequency. As we will show, there are several advantages utilizing information from multiple frequencies.

2) Nonlinear Inversion Method: Since wavenumber is nonlinearly related to the cross-spectral correlation, a typical nonlinear inversion method, such as Levenberg–Marquardt (LM) [31], can be used. The objective is to minimize the weighted squared difference between successive estimates of the modeled cross-spectral correlation when compared to the observations, i.e.,

$$\Delta C^{\tau}_{i,j,f} = \left\{\gamma_{i,j,f} C^{\mathrm{MODEL},\tau}_{i,j,f} - C^{\mathrm{OBS}}_{i,j,f}\right\} \tag{8}$$

where, at each iteration τ, the model–observation mismatch is weighted by the observed coherence. For the 1-D case, we cannot estimate the wave angle and, therefore, will only obtain estimates of the cross-shore component of the wavenumber. However, extension to two horizontal dimensions is straightforward (see Section III-C), given 2-D image sequences. Linearized models for the wavenumbers on the tomographic domain are solved iteratively as follows:

$$\begin{aligned} k^{\tau+1}_{f,m} &= k^{\tau}_{f,m} + \Delta k^{\tau}_{f,m} \\ \Delta k^{\tau}_{f,m} &= \left([R^{\tau}]^{T} R^{\tau}\right)^{-1} [R^{\tau}]^{T} \Delta C^{\tau}_{i,j,f} \\ R^{\tau} &= R^{\tau}_{i,j,m,f} \\ &= \gamma_{i,j,f}\sqrt{-1}D_{i,j,m}C^{\mathrm{MODEL},\tau}_{i,j,f}\Delta x. \end{aligned} \tag{9}$$

The model–observation mismatch is ordered as a column vector, with each element corresponding to a particular $i{-}j$ pair of observation locations. The matrix R describes the sensitivity of the cross-spectral correlation to the variation in each wavenumber in the tomographic domain. Thus, each column of R corresponds to the elements in the tomographic domain x_m, and each row corresponds to a $x_i{-}x_j$ spatial separation pair. It is possible to efficiently compute R by evaluating $C^{\mathrm{MODEL},\tau}$ at the observation locations. In the case where the predicted wavenumber updates $\Delta k^{\tau}_{f,m}$ do not converge (according to an *a priori* tolerance), the LM method diagonalizes R such that the minimization method is equivalent to gradient descent search.

Error predictions for the wavenumber estimates are computed as

$$(\varepsilon^{\tau}_{f})^{2} = \mathrm{diag}\left([R^{\tau}]^{T}[R^{\tau}]\right)^{-1}\left(\left[\Delta C^{\tau}_{f}\right]^{T}\left[\Delta C^{\tau}_{f}\right]\right)/\nu \tag{10}$$

where the degrees of freedom ν equals the sum of the coherences. This error prediction assumes that the errors in the wavenumber updates are normally distributed, and that the data are independent. The latter assumption is certainly not true, since data from a single observation location contributes to many observation pairs in the cross-spectral correlation estimate. However, the error predictions should provide good estimates of the relative error at different locations. Those locations with strong sample support $(D > 0, \gamma > 0)$ and strong sensitivity $(d/dk|C^{\mathrm{MODEL}}| > 0)$ will have the lowest error.

The nonlinear inverse method satisfies some important criteria for providing robust wavenumber estimates. First, it allows a spatially variable solution that can be applied to all available frequencies. Second, error estimates that reflect the sample design, the signal coherence, and the desired solution resolution are easily computed for use in assessing data quality. We therefore suggest this to be the most appropriate approach to wavenumber estimation in nearshore settings. The primary drawback to implementation of the method is additional computational complexity. However, this drawback can be handled using existing computational capabilities, including efficient matrix operations, multiprocessor computers, and ever-increasing memory.

3) Implementation Issues: Some final implementation issues are addressed here. They encompass choices that must be made about the analysis domain, which can have very different and typically coarser resolution properties compared to the image data. The tomographic resolution is a free parameter for any application of this methodology. The cost of high resolution is a larger sample design matrix D and a larger sensitivity matrix R. Both must be stored in the computer memory, and the latter must be squared and inverted. The cost of low resolution is an inaccurate representation of the spatial variations of the wavenumber. To balance these two costs, we chose to represent the wavenumber estimate with basis functions such that

$$k_i = \sum_{m=1}^{M} a_{i,m} k_m \tag{11}$$

where a k_m basis set is defined on a relative coarse domain, and $a_{i,m}$ represents smoothing weights used to project the basis set to an arbitrary location x_i. The smoothing weights can be any filter function. We used a Hanning filter

$$\begin{aligned} a(\delta_{i,m}) &= \{1 - \cos\left(0.5\pi[1+\delta_{i,m}]\right)\}^2, \qquad \text{if } r_{i,m} < 1 \\ \delta_{i,m} &= |x_i - x_m| L_x^{-1} \end{aligned} \tag{12}$$

where L_x is a smoothing lengths scale. A smooth solution requires $L_x > \Delta x_m$ (where Δx_m is the tomographic domain resolution). The sample design matrix must be modified to include the spatial correlation imposed by the basis function

$$D_{i,j,m} = \sum_{i'=i}^{j} a_{i',m}. \tag{13}$$

Additionally, to impose continuity on estimates in regions where there might be large data gaps, the sensitivity matrix R used in (9) was augmented with the basis autocorrelation such that $R' = R + \mu Q$ and $Q = [a_{m,m'}]^T a_{m,m'}$, where $\mu = 0.1$ was used. This solution balances minimizing the cross-spectral correlation errors against errors due to spatially erratic results that are associated with unresolved scales of the solution.

While the coarse resolution (Δx_m) of the tomographic domain should be designed to adequately resolve the bathymetry, it does not adequately resolve the much shorter scale of the wave phase variations. Using x_m directly in (5) would lead to integration errors in the model for the cross-spectral correlations. To solve this problem, the coarsely defined and smoothly varying wavenumbers on the x_m domain were interpolated to a much finer grid spacing of 1 m, using (11). Phases were then integrated to each observation location on this fine grid using (5).

Phase ambiguity remains to be a problem. A particular phase difference at large spatial separations might result from the integration over a large number of short wavelengths, or integration over a fraction of a larger wavelength. Mismatches between the observed and predicted phase of the cross-spectral coherence at these large lags may not be very useful in indicating whether a wavenumber estimate should be locally increased or decreased to improve the fit to the observations. Since the LM method assumes small phase errors, the coherence can be artificially reduced at long lags by applying a Hanning window mask (12) with a length scale parameter that adaptively depended on the wavenumber estimate: $L_m^\tau = 1/k_{\max}^\tau$, where $k_{\max}$ is the maximum computed wavenumber in the domain. The mask was applied to the sensitivity as $R'_{i,j} = R_{i,j} a_{i,j}$ (i.e., an element-wise multiplication, not convolution). We found that this approach worked well for initial wavenumber guesses that were either too high or too low. In principle, as the estimate converges, more distant sensor pairs may be allowed to contribute to the solution by increasing the length scale of the mask.

Finally, the iterative estimation scheme requires an initial wavenumber estimate. We suggest generating an initial estimate using linear wave theory and an estimate of the water depths.

III. Applications

A. Synthetic Example

To evaluate the suggested wavenumber estimation approach, we applied it to a synthetic data set. Cross-spectral correlations [Figs. 1(a) and (b) and 2(a) and (b)]were computed for two frequencies (i.e., 0.1 and 0.2 Hz) using linear wave theory to construct wavenumber profiles from a planar depth profile [Figs. 1(c) and 2(c)]. Random errors were included in the cross-spectral correlation by adding 50% random noise to the "true" wavenumber profile [Figs. 1(d) and 2(d)] and summing the resulting phases over 100 realizations. This combination of noise level and number of realizations produced cross-spectral correlations with a realistic coherence decay with increasing sensor separation distances. The phases were sampled at location x_j, with spacing Δx of 5 m. The cross-spectral correlation phases are, by definition, zero along the diagonal (i.e., where the signal from location x_j is compared to itself) and are antisymmetric about the diagonal ($\Phi_{ij} = -\Phi_{ji}$). The simulation shows that the wavelength is longer offshore (phase differences change slowly with spatial lags) and is shorter nearshore. The low-frequency (longer) waves are better resolved (broader coherence and clearly periodic phase structure) than the high-frequency waves (narrow coherence, random phase structure at large spatial separations).

Wavenumber estimates and corresponding error predictions were obtained using the nonlinear inverse method on a tomographic domain with spacing $\Delta x_m = 20$ m. We performed several experiments, including using all of the data, removing some of the sample data in a patch located between 50 m $< x <$ 100 m, and initializing the iterative method with wavenumbers that were too large and too small. Fig. 3 shows the estimation results applied to both frequencies. The estimated wavenumbers

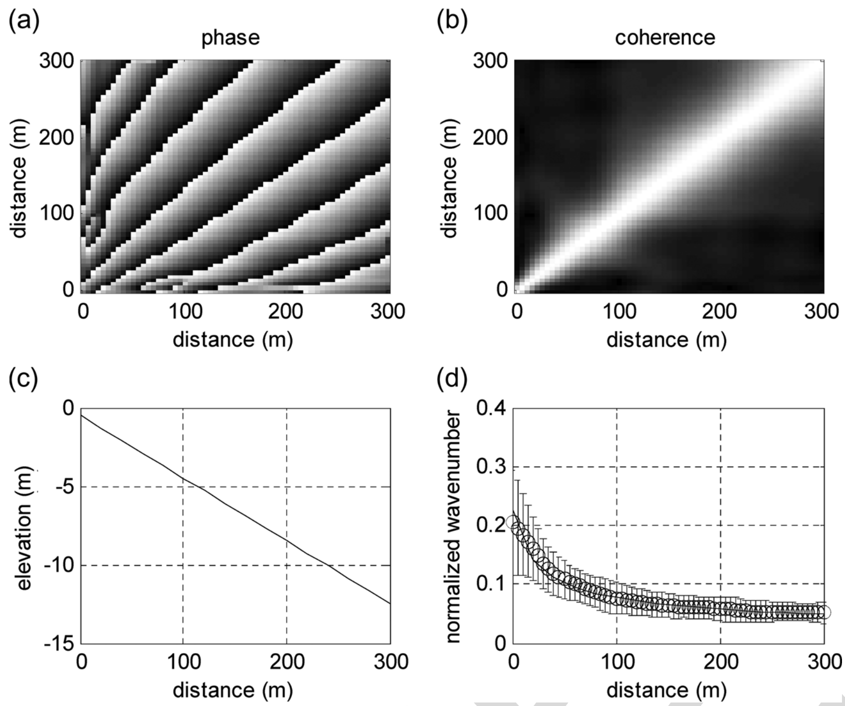

Fig. 1. Cross-spectral correlation (a) phase and (b) coherence for 0.1-Hz (10 s) wave propagation over (c) plane-sloping bathymetry. (d) Wavenumber samples were generated using linear wave theory plus a random variation. Error bars show one standard deviation. Wavenumbers are shown normalized by the sample spacing such that the Nyquist wavenumber occurs at a value of 0.5. Shading scale is (a) black $= -\pi$, white $= \pi$ and (b) black $= 0$, white $= 1$.

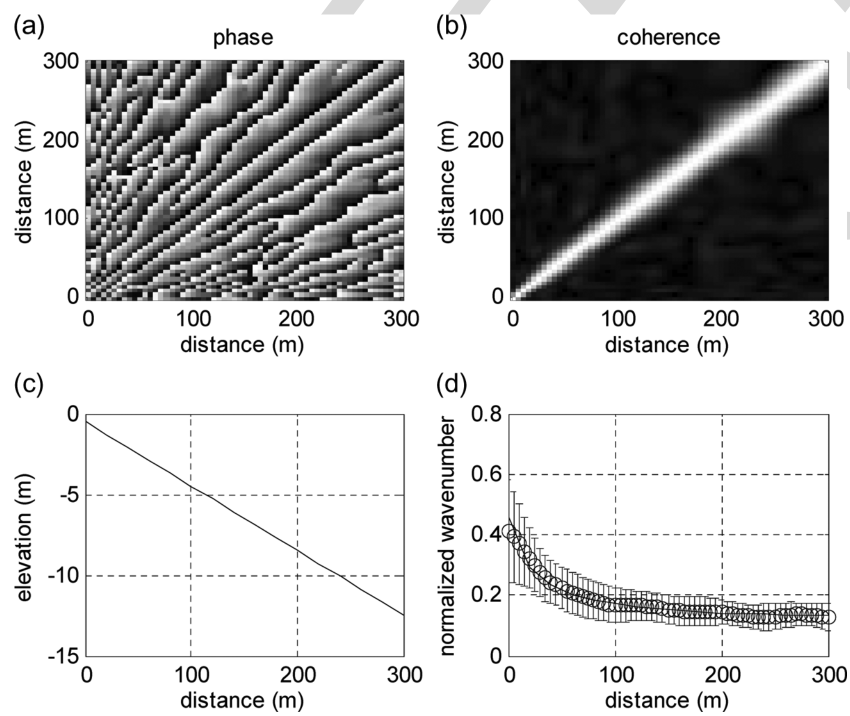

Fig. 2. Cross-spectral correlation phase and coherence for 0.2-Hz (5 s) wave propagation. Description of each panel is the same as in Fig. 1.

were very accurate at nearly all locations. At locations where the estimate was relatively inaccurate, such as near the location of the data gap, the error predictions (10) were also large. It is worth noting that the wavenumber estimate depends on the initial guess of the wavenumber in the region where data were missing. While such dependence on the initial guess is undesirable, the predicted errors correctly identify the region that is susceptible to the problem.

B. Field Data Example

We evaluated the nonlinear inversion method for wavenumber estimation using observations from a set of video cameras mounted on a tower at the U.S. Army Corps of Engineers Field Research Facility (FRF), Duck, NC. The cameras did not store full image frames (Fig. 4) during the study period, but instead, time series of intensity at a sparse set of spatial locations

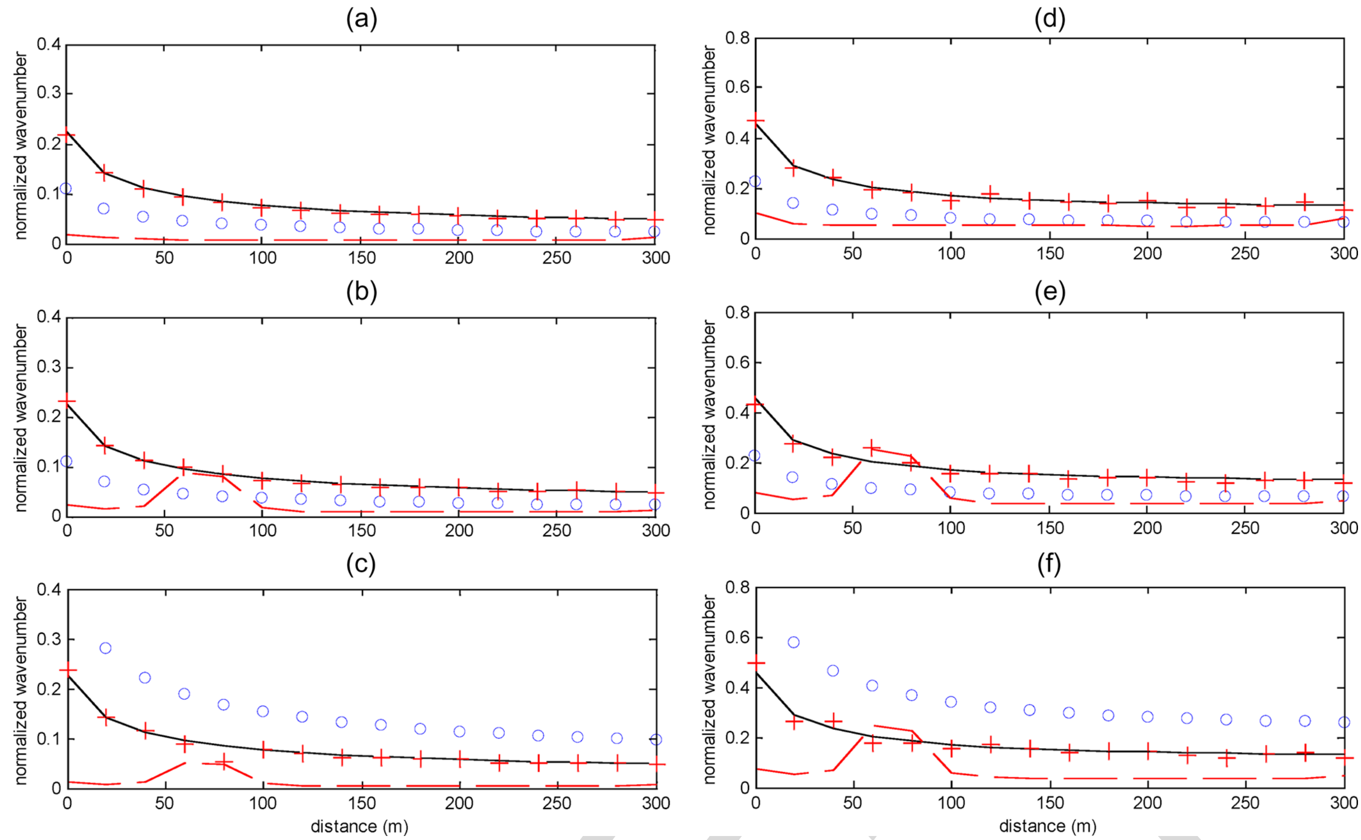

Fig. 3. Example wavenumber estimates using synthetic data for (a–c) a 10-s period and (d–f) a 5-s period. The estimation is started out with initial guess (circles) that is half the true value (a and d). The estimate $(+)$ is nearly identical to the true value (solid line). The rms error predictions (dashed line) are larger for the less well-resolved 5-s period data. In the second experiment (b and e), a 50-m patch of the observations was removed between $50 < x < 100$ m. In the third experiment (c and f), the initial guess is twice the true value.

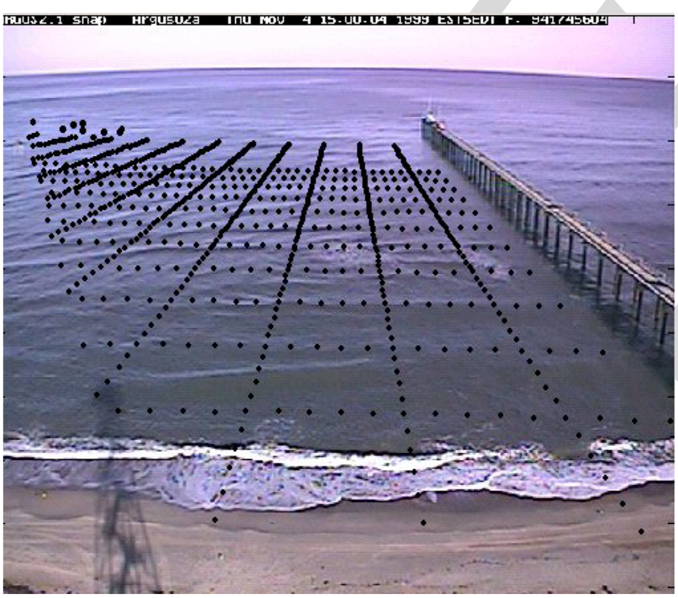

Fig. 4. Camera view of the Duck field site, showing the image time series sample locations (black dots). The camera orientation and distortion are used to map the data to georeferenced locations. The cameras are mounted on a tower, whose shadow on the beach provides a self-portrait.

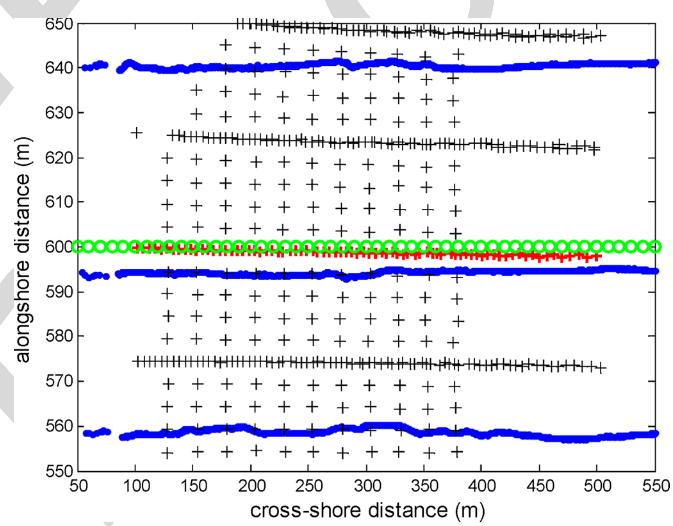

Fig. 5. Duck sampling pattern with the shoreline at the left near $x = 100$. Bathymetric survey locations are indicated by dots (very densely spaced in the cross-shore direction); image time series $(+)$ were sampled over the 2-D domain. The samples used in the 1-D analysis are indicated with bold symbols. Wavenumbers were estimated on a sparse tomography domain, which is indicated by circles (1-D case).

were retained for analysis (Fig. 5). This sampling scheme was implemented to balance data storage constraints against the requirements for resolving the important components of the incident wave field. With a cross-shore sample spacing of about 5 m, waves longer than 20 m (half the Nyquist wavenumber) should be well resolved. This corresponds to waves with a period longer than 6 s at a water depth of 1 m. At the Duck field site, the annual mean wave period is about 8 s, which means that a depth of 1 m, these waves have a 25-m wavelength

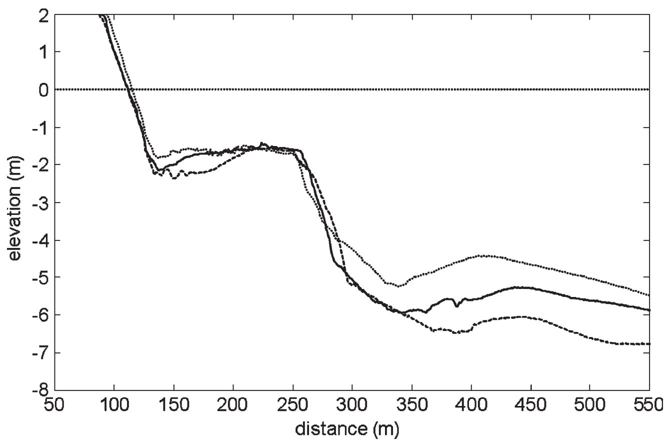

Fig. 6. Cross-shore bathymetry transect surveyed on November 4, 1999, at an alongshore location near 600 m (solid line), 560 m (long dash), and 640 m (short dash).

and are well resolved. With this array design, these waves are resolvable until water depths reach about 0.75 m. Thus, for this field site, and depending on tidal height, wavenumber estimates should be possible for the region offshore of about $x = 120$ m (Fig. 6).

As in the synthetic example, we chose a cross-shore resolution of $\Delta x_m = 20$ m for the tomographic domain and a corresponding smoothing scale of $L_x = 40$ m. At the FRF, ground-truth bathymetry data were obtained from a three-wheeled (10-m footprint) survey vehicle, called the Coastal Research Amphibious Buggy [32]. The ground-truth bathymetry along the 1-D cross-shore transect (Fig. 5, middle) that is used in this analysis is shown in Fig. 6. It includes a very steep swash zone (near $x = 120$ m), an inner sand bar ($x = 230$ m), and an outer sand bar ($x = 450$ m). While the remote sensing data extend from 100 m $< x <$ 500 m, we estimate the wavenumber both onshore and offshore of this extent. The error predictions should indicate the locations where robust wavenumber estimates are available.

Using the pixel array data collected on November 4, 1999, at approximately 20:00 GMT, the sample cross-spectral correlation (4) was computed at a series of frequencies ranging from 0.07 Hz (15-s wave period) to 0.23 Hz (4-s wave period). The record length was 68 min, and the sample interval was 0.5 s. The band-averaged frequency resolution was 0.03 Hz, with 136 nonoverlapping frequency samples used in each band. The phase and coherence are shown in Fig. 7 for each sample frequency. Only the lower portion of the symmetric correlation matrix was computed and stored. Spatial coherence, summed over all spatial separations, was highest at 0.167 Hz (6 s), followed by 0.10 Hz (10 s), and then 0.2 Hz (5 s) (Table I). We expect that these frequencies will yield accurate wavenumber estimates if the corresponding wavenumber structure is spatially well resolved. Note that the peak wave energy does not necessarily correspond to the peak coherence. In this case, the peak wave period based on sea surface height measured 8 m offshore was 8.9 s (0.11 Hz); the peak direction was 24° south of the shore normal; and the significant wave height was 0.5 m.

The nonlinear inverse estimation method was applied to the sample cross-spectral correlations at each frequency over

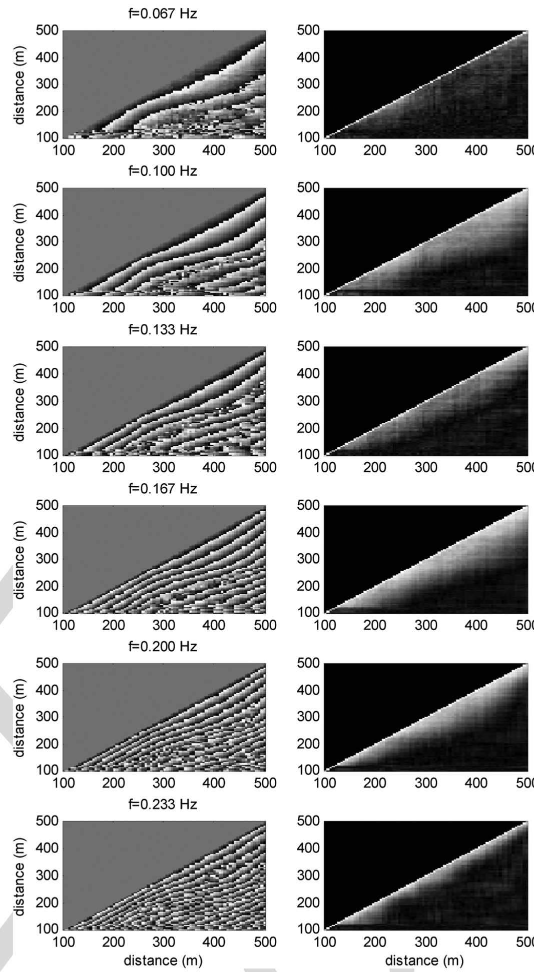

Fig. 7. (Left column) Phase and (Right column) coherence for individual frequencies determined from pixel array data (Duck, NC).

TABLE I
COHERENCE AND WAVENUMBER ERROR STATISTICS

Frequency (Hz)	Total Coherence	RMS wavenumber error (m^{-1})
0.067	609.051	0.020
0.100	999.266	0.026
0.133	748.390	0.034
0.167	1052.162	0.048
0.200	855.658	0.053
0.233	638.458	0.068

the entire array. To initialize the iterative method, at each frequency, a linear dispersion model was used (assuming shore-normal wave incidence) to generate initial wavenumbers at each location x_m. We used a bathymetry with a constant depth of 1 m for the initial guess.

For the purpose of comparison, linear wave theory was used to compute the "true" wavenumber for each frequency. The measured bathymetry and tide level at the time of the image collection was used. (We acknowledge that linear wave theory gives an imperfect ground-truth for parts of our analysis domain [20].) Fig. 8 shows the comparison of the "true" and estimated wavenumbers. The rms mismatch between the "true" and estimated wavenumbers was computed by using the predicted errors as weights. Thus, locations where the predicted

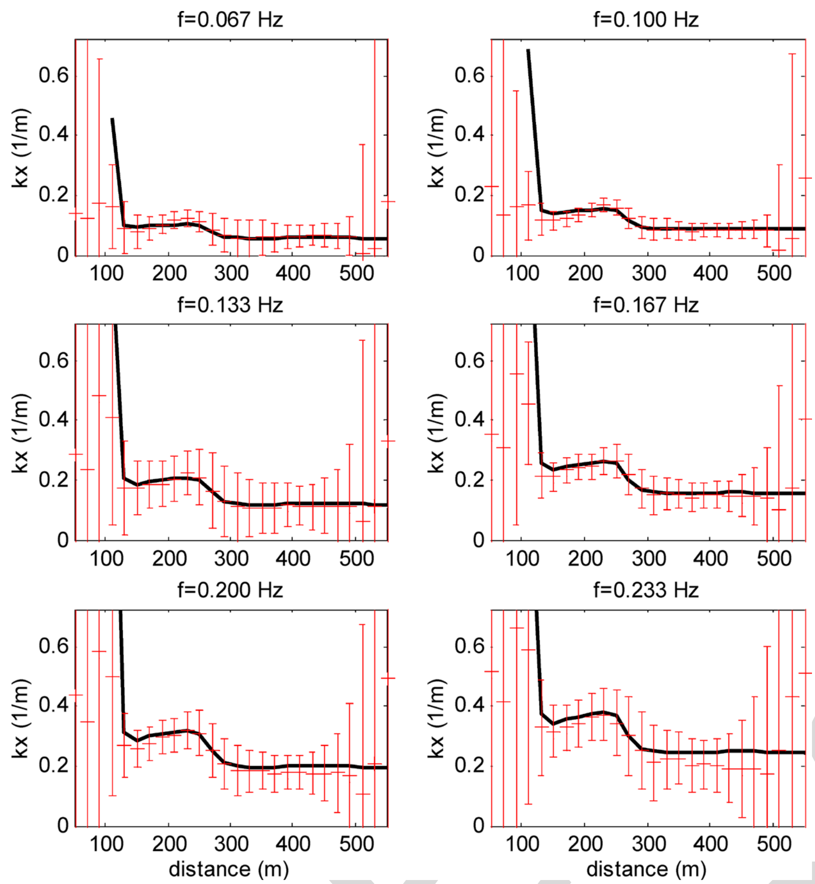

Fig. 8. Wavenumber estimates using Duck data. Error bars show the rms error prediction. Solid line shows linear wave theory prediction for each frequency.

errors (shown as error bars) were relatively high did not contribute as much to the rms error. The best estimates (Table I) were obtained for the lowest frequency (0.067 Hz, rms error 0.02 m^{-1}). This is a bit surprising, given the low coherence at this frequency. However, these waves are relatively long, and their spatial structure is well resolved by the sample design. The three frequencies with largest spatial coherence also had relatively low rms errors. Importantly, the spatial distribution of the predicted errors reflected the locations having high-quality data. Overall, the estimated wavenumbers were correlated to the "true" values with $r^2 = 0.96$ and a slope of 1.0 (Fig. 9).

C. Applications in 2-D

The wavenumber estimation methods based on fitting the cross-spectral correlation can be extended to a 2-D domain. This allows the wave direction to be included as an unknown parameter. Drawbacks of such an extension are given as follows: 1) the number of unknown variables is doubled (and this quadruples the computational effort for the wavenumber estimation procedure) and 2) the dimension of the cross-spectral correlation matrix is approximately squared, increasing both computational effort as well as memory requirements for the data analysis procedure. For example, the 2-D pixel array in the field data application included 1124 sample locations, yielding 632 250 useful cross-spectral correlation elements, each with a real and an imaginary component, at each of the six sample frequencies. The result is 7.5 million data values. It should be noted that the spatial extent of this sampling array is not unusually large, as it spans only a few hundred meters alongshore. Many useful applications could extend at least several to tens of kilometers alongshore. To overcome the data management hurdles, we solve the inverse problem locally over spatial regions where we assume the wavenumber and direction to be slowly

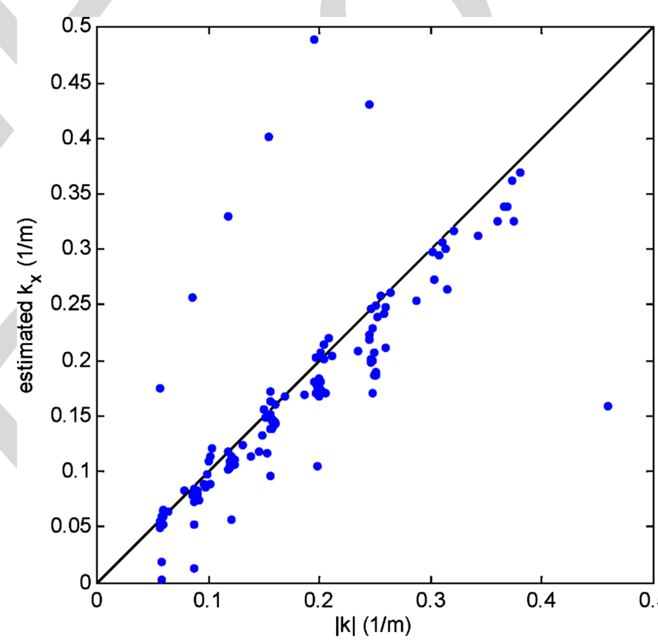

Fig. 9. Comparison of estimated and "true" wavenumbers [correlation coefficient $= 1.05$ and skill$(r^2) = 0.96$]. Data represent all analyzed frequencies and all locations in the tomographic domain.

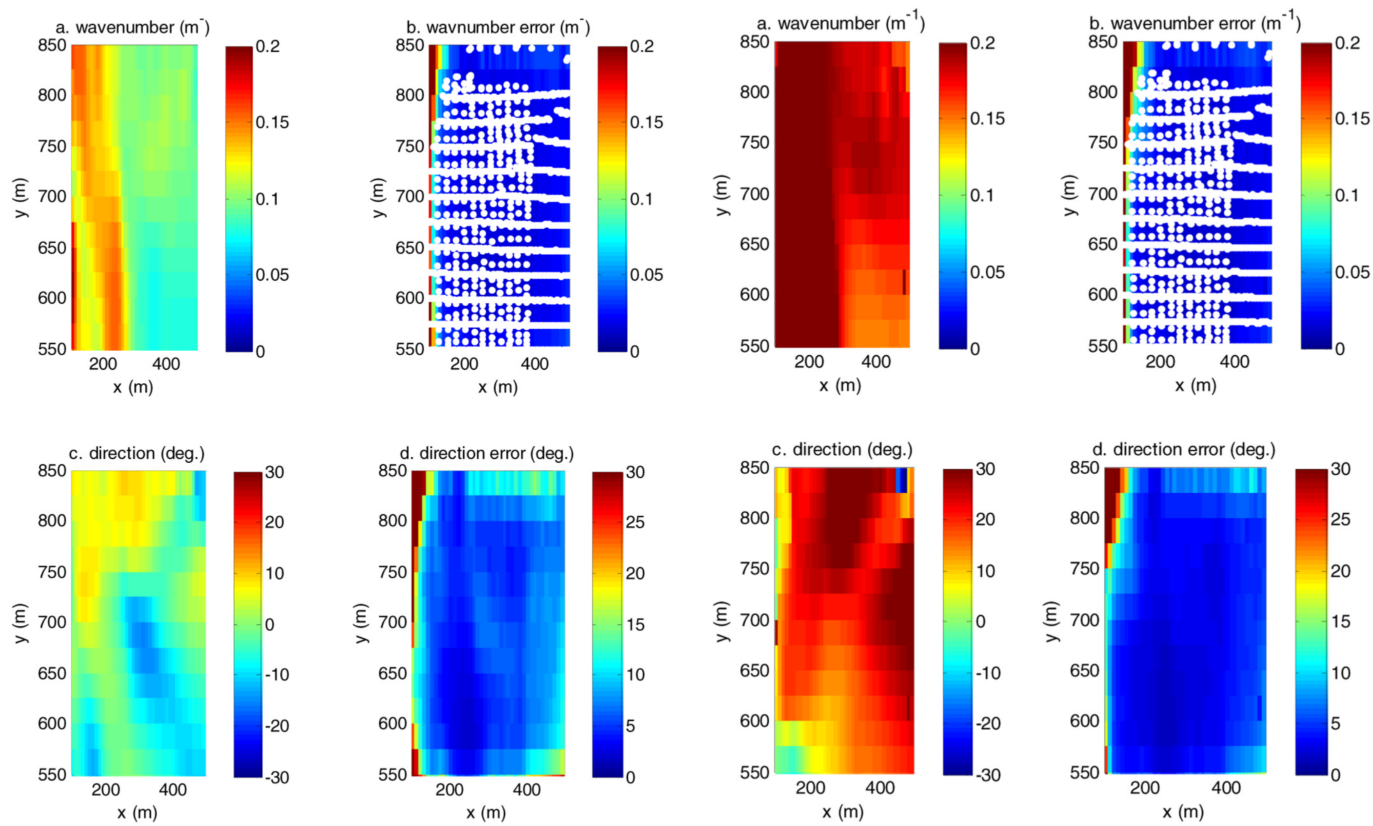

(a) (b)

AQ6 Fig. 10. (a) Estimates of (a) wavenumber magnitude and (c) wave direction and (b, d) predicted errors at a frequency of 0.10 Hz (10-s wave period). The median direction at the seaward boundary was -5° (waves approach from the south, but nearly shore normal). White dots on the wavenumber error prediction plot indicate image pixel sample locations. (b) Estimates of wavenumber magnitude and wave direction and predicted errors at a frequency of 0.167 Hz (6-s wave period). The

4/C median direction at the seaward boundary was $+29^\circ$ (waves from the north).

varying. That is, we solve the problem at one spatial location at a time (i.e., with $M = 1$) rather than solving for wavenumbers at all locations simultaneously. Then, we move the analysis to each element of the tomographic domain. The revised approach still benefits from resolving both the frequency and spatial dependence of the cross-spectral correlation without having to assume a locally homogeneous bathymetry.

Fig. 10(a) and (b) shows the analysis of a 2-D domain. The results are plotted for two different frequencies (0.10 and 0.167 Hz). Fig. 10(a) (0.10 Hz) shows that the wavenumber is robustly estimated in much of the domain, indicated by error predictions that are much smaller than the minimum wavenumber. Errors are larger along the shoreline near $x = 100$ m. At the offshore boundary, the direction of wave approach varies somewhat but is generally close to shore normal. The median direction along the offshore boundary was -5° (waves approaching slightly from the south); the median direction over the whole domain was -1°; and the median directional uncertainty was 7°. Fig. 10(b) (0.167 Hz) shows that wavenumber is, again, robustly estimated. At the offshore boundary, the direction of wave approach was clearly from the north. The median direction along the offshore boundary was 28° (waves approach from the north); the median direction overall was 20°; and the median directional uncertainty was 4°. Fig. 11 shows independent estimates of the frequency- and direction-resolved spectrum obtained from an array of pressure sensors located 900 m offshore at a water depth of 8 m [33]. It shows the same differences in approach directions for the two frequencies presented in Fig. 10(a) and (b). For both frequencies, the directions estimated from the pressure sensors have larger magnitudes than the image-derived directions. This is consistent with effects of refraction over the 400-m propagation distance between the gage and the seaward boundary of our estimation domain. Correcting for refraction (symbols plotted in Fig. 11) significantly improves the comparison between the image- and pressure-based wave direction estimates.

D. Application to Bathymetry Inversion

While the wavenumber estimates are directly useful for characterizing the wave directional distribution and for testing wave dispersion relationships, a key motivation for this effort is to facilitate robust remote-sensing-based bathymetry estimation. Bathymetry estimation requires a solution of yet another inverse problem using a dispersion model that relates wavenumber to water depth. We use linear wave theory, i.e.,

$$(2\pi f)^2 = gk\,\tanh(kh) \rightarrow k = \text{funct.}(f, h) \qquad (14)$$

where g is the gravitational acceleration, and h is the local water depth. Given values for f (i.e., sample frequencies) and h (a guess at the correct depth), this equation can be

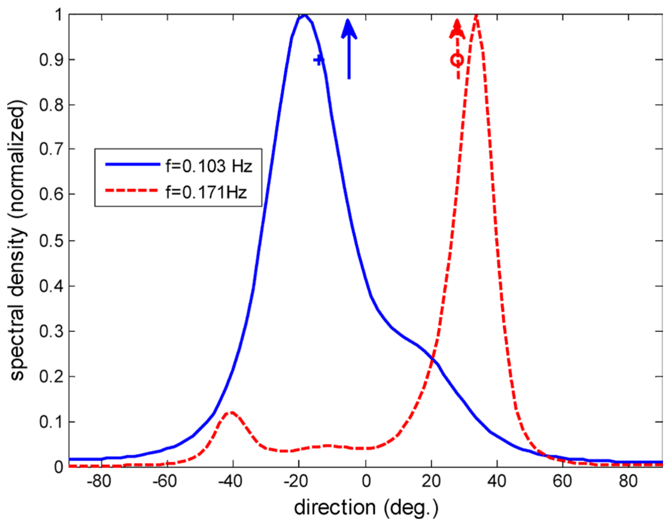

Fig. 11. Slices from directional wave spectrum based on *in situ* measurements at a water depth of 8 m. The two frequencies closest to 0.1 and 0.167 Hz were selected. Peak directions were -18 (0.1 Hz) and 34° (0.17 Hz). The refracted peak directions were computed for shoaling from a depth of 8 m to a depth of 5 m and are shown with symbols (+ for 0.1 Hz and ○ for 0.167 Hz). The arrows indicate the median direction at the offshore boundary corresponding to the 2-D wavenumbers of the motion imagery analysis.

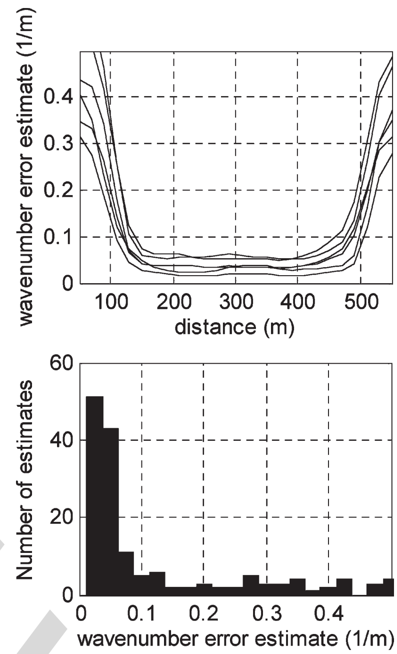

Fig. 12. Wavenumber error predictions and histogram.

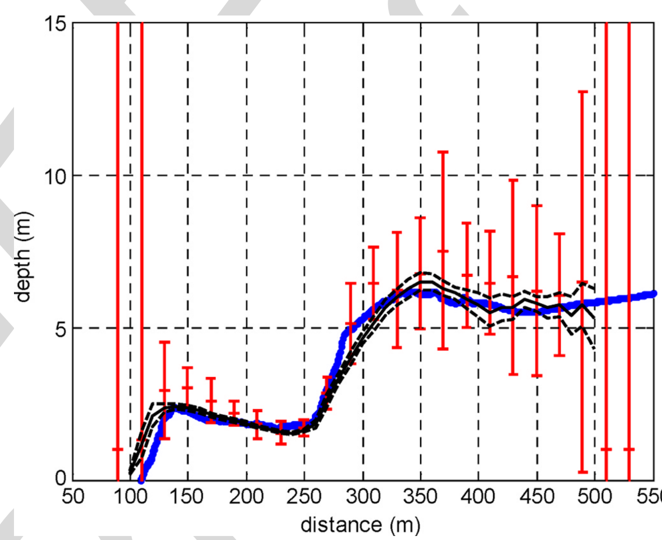

Fig. 13. Water depth estimated from image-derived wavenumbers. The estimates from the 1-D wavenumber inversion are shown with error bars and the estimates from the 2-D analysis are shown as a solid line with dashed lines, indicating one standard deviation error. The nearest survey observations are shown as blue dots.

solved for wavenumbers (it is a transcendental equation, solved iteratively). We use the LM method to solve for the value of h that minimizes the error between the wavenumber predicted by (14) and that estimated from the imagery via (9). The advantage of separating the bathymetry inversion from the wavenumber inversion is that the quality of the image data can be objectively evaluated. Data with large errors can be rejected outright, or the errors can be used as weights in the inversion scheme, just as the coherence was used in (8). Furthermore, since each frequency is independent of the others, the depth inversion applied at each spatial location uses a number of independent wavenumber estimates. This should result in quantitatively accurate bathymetric error predictions, because the number of degrees of sampling freedom will not be overestimated. Otherwise, cross-spectral correlation estimates are not independent because data from each pixel are utilized multiple times as they is compared to itself and all the other pixels. Another reason for separating the wavenumber estimation from the bathymetry estimation is that the sensitivity of wavenumber to depth is very high in shallow water and is zero offshore. The near-zero sensitivity at the offshore region will destabilize a global bathymetry inversion, whereas this does not affect the wavenumber estimation problem.

The wavenumber error predictions obtained from the nonlinear inversion can be used to identify thresholds used to reject or weight the wavenumber estimates when applied to the depth inversion problem. Fig. 12 shows the spatial distribution of the errors and the error histogram from all the locations and frequencies. There appears to be a minimum error of approximately 0.05 m^{-1}. Thus, errors that are much larger than this value indicate relatively low-quality data. Using a Gibb's energy analogy [27], weights applied to the depth inversion were computed as $E = \exp(-\varepsilon/\kappa)$, where κ was 0.02 m^{-1}, and ε is the error prediction (as long as $\kappa < 0.1$, the choice of κ was not too important). The weight E is largest for error predictions approaching the minimum error, and E is small for larger errors.

Fig. 13 shows the resulting water depth estimates based on the 1-D (cross-shore) estimates of the wavenumber. Skillful depth estimates are obtained from depths between 2 and 6 m. The prediction is most accurate over the sandbar, where the mismatch between surveyed and estimated bathymetry is less than 10 cm, and the predicted errors are also small. Seaward of about 300 m (depths > 5 m), the bathymetry estimate is less accurate, and the error predictions are larger. Near the shoreline, the wavelength is short and poorly resolved; wavenum-

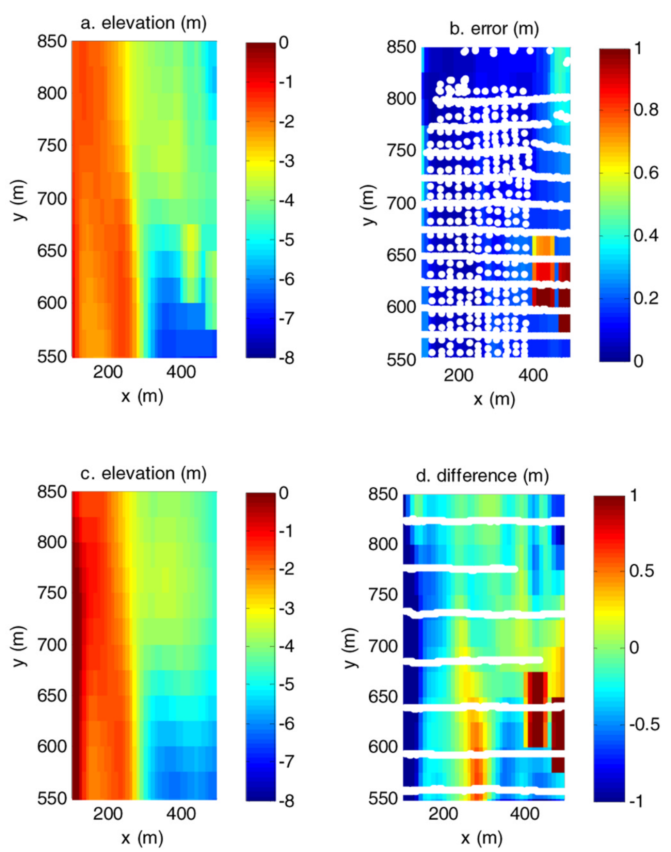

Fig. 14. Comparison of bathymetry derived using (a) 2-D wavenumber estimates and (c) surveyed (and spatially interpolated) bathymetry. Maps show (b) the predicted errors from the wavenumber inversion and (d) the actual differences between wavenumber inversion and survey. White dots on the error maps indicate the sample locations for both (b) imagery and (d) survey data sets.

4/C

ber error predictions are large, and the bathymetry estimate is poor.

The differences between the predicted and true bathymetries are not random. Offshore, the predictions are too deep. This is likely due to neglecting the wave direction for the 1-D analysis and interpreting the cross-shore wavenumber component as the wavenumber magnitude that appears in (14). In essence, the cross-shore wavenumber is too small, and the depth is overestimated. Near the shore, the bathymetry predictions are, again, too deep. This could result from neglecting the alongshore component of wavenumber, or it could be due to wave nonlinearity wherein waves travel faster than predicted by linear dispersion, and the resulting wavenumbers are smaller than expected. The offshore wave height of 0.5 m at the time of the analysis would lead to wave breaking at a water depth of roughly 1 m; hence, there was very little breaking over the bar—as evident in Fig. 4. Other mechanisms for causing discrepancies, such as setup or strong wave–current interactions are not likely to be too important because of the lack of wave breaking to force them.

Using the wavenumbers from the 2-D analysis to estimate the bathymetry (Figs. 13 and 14) results in shallower (and mostly improved) bathymetry both offshore and at the shallower portions of the profile, suggesting that refraction was, indeed, largely responsible for the discrepancies observed in the 1-D analysis. Larger errors in the middle of the 2-D region appeared where there was strong alongshore bathymetric variability (Fig. 4). This variability was not allowed by the smoothing properties inherent in the 2-D analysis approach.

IV. Discussion

A. Comparison to Other Methods

The proposed tomographic approach utilizing cross-spectral correlations from coastal imagery resolves spatial and frequency variability of the wavenumber field and includes error estimates that can be used to appropriately weight the wavenumber estimates. The proposed approach comes with a larger computational effort than other formulations. Is it worth the effort? The formulations given in (1)–(9) show that the theoretical underpinnings of all of the coherence-based wavenumber estimation approaches are equivalent. Therefore, applying each method to the 1-D test example should yield similar results. Differences between methods will result from the way that each approach rejects observation noise through smoothing at the expense of spatial, frequency, or direction resolution. Since we do not know the "true" answer (except through forward modeling from the surveyed bathymetry), this analysis will not necessarily identify the approach that is most accurate.

1) Time Delay Approach: We use the method described in [26] to filter the cross correlation (3) to estimate the time delays between different sample locations. Fig. 15 shows the resulting time delays between all sample pairs and the correlation at each delay. Immediately apparent is the rapid decorrelation with spatial separation. Nonetheless, time lag estimates are accurate compared to "true" values derived using the known wave speed via (2). The advantage of the time delay approach is that the phase ambiguity problem is minimized. This is particularly true in natural systems where the generally broad-band random waves will guarantee that a single time delay will maximize the correlation between sensors. (In laboratory settings with monochromatic waves, strong correlations can be found at lags that are multiples of the wave period.) Fig. 15 shows the phase ambiguity appearing for time lags exceeding 20 s (or about three cycles of the dominant 6-s wave period). A problem with the time delay approach is that it is not clear how the quality of the time delay estimates based on the correlation, which is exceeding low at many relevant lags, is identified. Nonetheless, we computed the wavenumber via an inverse solution of (2). [Inverse solutions of (2) are, in principle, linear and do not require iterations.] Fig. 16 shows wavenumber estimates based on the time delays. In the middle of the computational domain, the results are more or less equivalent to those in Fig. 8 at $f = 0.167$ Hz.

Another problem with the time delay approach is that comparisons to predictions from a wave dispersion equation (or its inverse) require specification of a dominant wave period. In the cross-spectral correlation methods, wave period (or frequency) is an independent variable, not a required input variable. The dependence of time delays for different wave

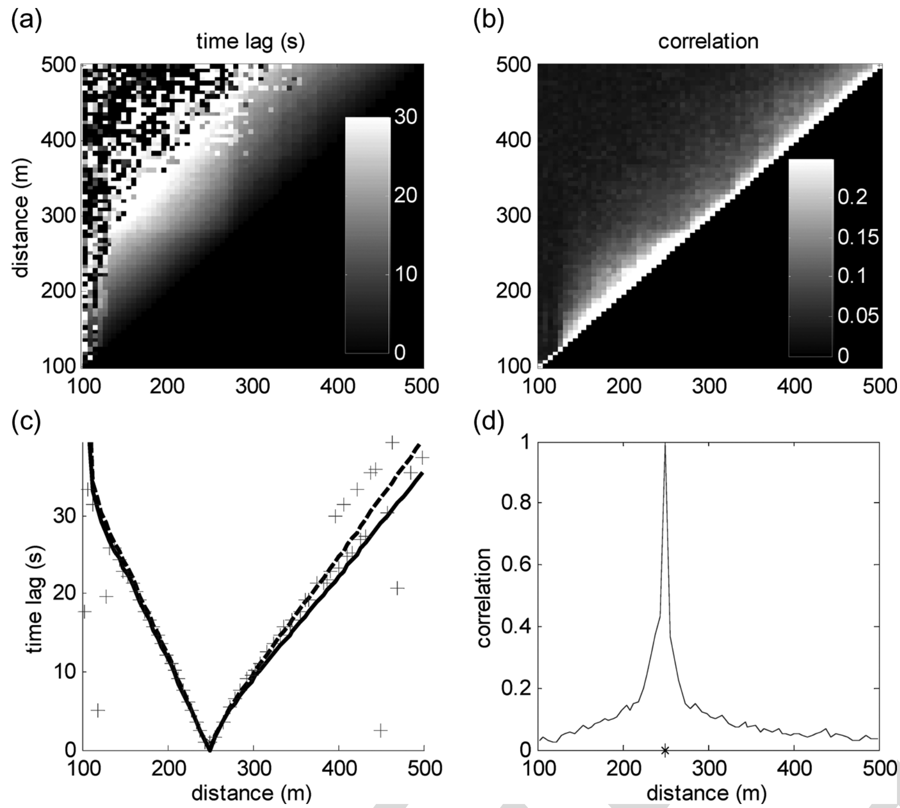

Fig. 15. (a and c) Time lag estimates and (b and d) associated correlation for all sensor pairs (top row) and for a slice comparing all sample locations to the location $x = 250$ m. The dashed line is the predicted time lag using the full dispersion equation at $f = 0.167$ Hz, and the solid line is the nondispersive shallow-water approximation.

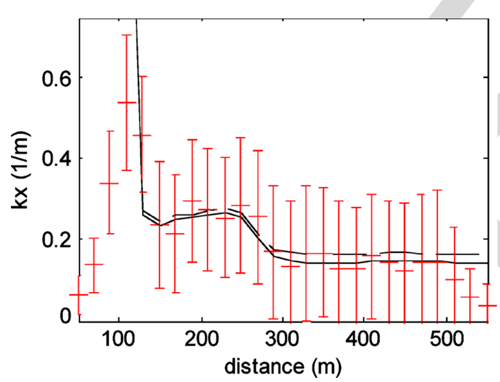

Fig. 16. Wavenumber estimate (and rms error prediction) using time lag data (assuming $f = 0.167$ Hz) compared to the linear wave theory prediction. The solid line is the theoretical prediction for nondispersive waves, and the dashed line is theoretical prediction for dispersive waves.

periods shows that there could be considerable time delay dependence on wave period (dashed line in Fig. 15), and that these errors accumulate at large spatial lags.

2) Single-Mode (EOF) Approach: Given that the proposed nonlinear estimation routine worked well in the test case, we suspect that, due to the long time series and high coherence at several frequencies, the single-mode EOF approach would also be effective. Fig. 17 shows the results of that approach. The results are very good, with a few exceptions. There is clearly more short-scale variability in the EOF estimate, which did not include any smoothness constraint. Simple spatial filtering would achieve a smoother result. However, the EOF wavenumber estimate is clearly unstable in a few locations at frequencies with relatively low coherence. Unfortunately, there is not a clear method to identify the errors. There is no reason to restrict the EOF analysis to a single frequency, and therefore, consistency of estimates across a few frequencies may be used to provide improved uncertainty estimates, particularly if the results are used for bathymetry inversion. Furthermore, if there are multiple dominant wave trains at a single frequency, the EOF method could be applied to separate them as a preprocessing step to the nonlinear estimation approach.

B. Spatial Resolution

It is important to identify the spatial resolution of the wavenumber estimator presented in this analysis. Nearshore, spatial variations in the incident wavenumber (i.e., k_{wave}) result from corresponding variations in the bathymetry. The scale of the bathymetric variations might be shorter or longer than the wave scale, and they might be shorter or longer than what can be resolved by the sampling scheme.Intuitively, it AQ7 seems reasonable that we can resolve bathymetric variations that are much longer than the incident wavelength. Can we resolve bathymetric variations that are shorter than the incident wavelength? How well must we resolve the incident waves?

To illustrate this problem, consider a flat seabed to which small sinusoidal bathymetric perturbations are added. The flat bottom yields a constant incident wave wavenumber k_{wave}. If the bathymetric perturbations are small, then the wavenumber is modulated as $k(x) = k_{\text{wave}}(1 + \beta \cos[2\pi x k_{\text{bathy}}])$, where k_{bathy} is the wavenumber of the bathymetric perturbation, β

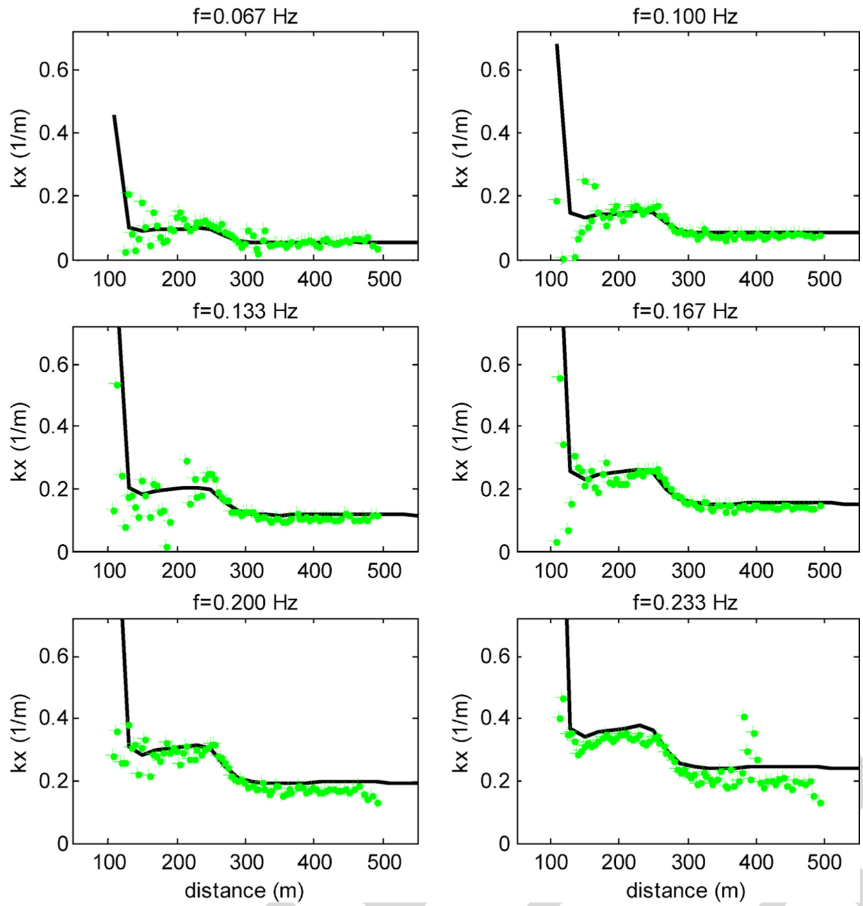

Fig. 17. Comparison of wavenumber estimates using the singular value method (+) to the linear wave theory prediction at each sample frequency (solid line).

is the resulting (small) amplitude of that perturbation relative to the undisturbed wavenumber. Inserting a modulated wavenumber into the equation for the cross-spectral correlation (5) yields (e.g., the imaginary component)

$$\begin{aligned}\Im[C] &= \sin\left(2\pi\Delta x k_{\mathrm{wave}}\left\{1+\beta\,\cos[2\pi\Delta x k_{\mathrm{bathy}}]\right\}\right)\\ &= \sin(2\pi\Delta x k_{\mathrm{wave}})\\ &\quad+\frac{\beta k_{\mathrm{wave}}}{2k_{\mathrm{bathy}}}\sin\left(2\pi\Delta x[k_{\mathrm{wave}}+k_{\mathrm{bathy}}]\right)\\ &\quad-\frac{\beta k_{\mathrm{wave}}}{2k_{\mathrm{bathy}}}\sin\left(2\pi\Delta x[k_{\mathrm{wave}}-k_{\mathrm{bathy}}]\right)\\ &\quad+o(\beta^2). \end{aligned}\tag{15}$$

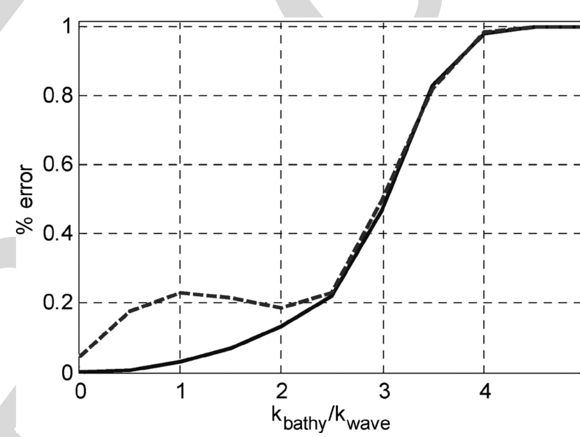

Fig. 18. Sensitivity of wavenumber estimation errors to bathymetric perturbation length scales k_{bathy}, normalized by the surface wavenumber k_{wave}. The two lines show the sensitivity for the case of no measurement noise (solid) and 10% noise (dashed). Other parameters were $k_{\mathrm{wave}} = 2\pi/25\ \mathrm{m}^{-1}$, $\Delta x = \Delta x_m = 2.5$ m, and $L_x = 5$m.

The interaction of the incident wave signal and the bathymetric signal produces two scales of variability (as a function of spatial lag Δx) in addition to the wave scale. There is a longer scale response associated with the difference between the incident and bathymetric wavenumbers and a shorter scale response associated with their sum. The response of these contributions is linearly damped as k_{bathy} increases relative to k_{wave}.

This simple example indicates that there are several factors that affect the ability to resolve short-scale bathymetric features. First, these features modulate the cross-spectral correlation most strongly when they are long compared to the incident wavelength (i.e., small values of $k_{\mathrm{bathy}}/k_{\mathrm{wave}}$). In practice, there is an additional damping of short features due to the spatial filtering that is imposed by our analysis. Fig. 18 shows the percent error associated with attempts to retrieve sinusoidal perturbations of the incident wavenumber. Synthetic cross-spectral correlation samples were generated from perturbed wavenumber profiles. In the second example, 10% percent noise was added to the "true" perturbed wavenumber profile. In the case without noise (Fig. 18, solid line), the retrieval errors are less than 20% for $k_{\mathrm{bathy}}/k_{\mathrm{wave}} < 2.5$. The error climbs rapidly for higher bathymetric wavenumbers due to the smoothing filter that completely removes features with a scale equal to the Nyquist wavenumber ($k_{\mathrm{Nyq}} = \pi/\Delta x_m$ or $k_{\mathrm{Nyq}}/k_{\mathrm{wave}} = 5$).

In the more realistic scenario where 10% percent noise was added to the observations (Fig. 18, dashed line), the error sensitivity is different. There is a local peak in the retrieval error at $k_{\mathrm{bathy}}/k_{\mathrm{wave}} = 1$. This occurs because the difference wavenumber term in (15) is zero, and only the sum wavenumber contributes to the signal. The sum wavenumber (shorter wavelength) is not well resolved by the sample spacing, and consequently, the perturbation is not well estimated. As k_{bathy} increases, the retrieval error slightly decreases because the difference wavenumber term, which is well resolved, once again contributes to the signal. Finally, further increases in k_{bathy} are not resolved as the smoothing filter again dominates the error.

There is a fortuitous relationship between sampling resolution capabilities and typical estimation requirements. Shorter scale bathymetric features are found in the shallowest waters where waves are most sensitive to depth variations. Since shore-based imaging typically has higher resolution closer to the shoreline, the short wavelength signals of interest are most likely to be resolved. In deep water, the length scales of bathymetric features are longer; the wavelengths that are sensitive to depth variations are also longer; and these longer scales still ought to be resolved by the shore-based sensor. As a rule-of-thumb (assuming measurement noise is unavoidable), the shortest (cross-shore dimension) resolved bathymetric feature will be about twice the wavelength of the incident waves that are resolved by the imaging system. Allowing that nearshore waves are inherently depth dispersive, which implies that $k_{\mathrm{wave}}h \leq 1$, this suggests that bathymetric features must be longer than about ten times the water depth. For average water depths of several meters, features that are tens of meters long are, in principle, resolvable. This resolution is about ten times better than what is achievable with the energy density identification approach [15], even with a similar pixel resolution (1–2 m), mainly because the assumption of a locally homogeneous bathymetry over the sampling array region is not required in the proposed method. The tradeoff is that the present approach only resolves a single dominant wavenumber, while the energy density approach resolves many different wavenumbers. The latter approach may perform better in the case of a directionally bimodal or very directionally broad-banded incident wave spectrum where the assumption of a single dominant wavenumber may be overly simplistic.

V. Conclusion

We have reviewed several approaches that have been used to estimate ocean surface gravity wavenumbers from wave-resolving image sequences. Two fundamentally different approaches exist that utilize this type of data. A power spectral density approach identifies wavenumbers that maximize image intensity variance. Alternatively, a cross-spectral correlation approach identifies wavenumbers that maximize intensity coherence. The first method finds, at an arbitrary wavenumber, the frequency associated with maximum spectral density. This approach requires application of a 2- or 3-D FFT to, typically, full frame images. The spatial resolution of the wavenumber estimates is typically $O(100)$ times the image pixel resolution.

The second approach finds, at each resolved frequency, the wavenumber that maximizes the observed cross-spectral coherence. Numerous solution methods have been suggested for this approach, including cross correlation and empirical orthogonal function analysis. Here, we developed a solution based on a tomographic analysis that utilizes a nonlinear inverse method and may be applied to both time- and frequency-domain analyses. We demonstrate that a formal treatment of the problem leads to a nonlinear inverse problem that can be solved to yield robust wavenumber estimates and error predictions.

We expand in detail a frequency-domain solution approach that yields robust retrievals of wavenumber estimates from the imagery. The approach is tolerant to noise and other forms of sampling deficiency and can be applied to arbitrary sample patterns, as well as to full frame imagery. The approach provides error predictions that are useful for quality control and subsequent applications to, for instance, bathymetry estimation. A quantitative analysis of the resolution of the method indicates that the cross-spectral correlation fitting approach has about ten times better resolution than the power spectral density fitting approach. Furthermore, the resolution analysis provides a rule of thumb for bathymetry estimation: Cross-shore spatial patterns may be resolved if their length is ten times the water depth. This guidance can be applied to sample design to include constraints on both the sensor array (image resolution) and the analysis array (tomographic resolution). Finally, the method supports bathymetry estimation through inversion of a wave dispersion model. It does this by providing robust statistically consistent and independent wavenumber estimates at multiple wave frequencies.

Acknowledgment

The authors would like to thank the Beach Wizards who contributed to the development of this effort. The authors are particularly indebted to P. Catalan for the encouragement, evaluation, and critical review. Comments from an anonymous reviewer considerably improved the clarity of the manuscript. Finally, we could not have performed a sensible field evaluation without the stage set by both the Army Corps of Engineers' FRF and R. Holman's Argus program.

References

[1] R. A. Holman and J. Stanley, "The history and technical capabilities of Argus," *Coast. Eng.*, vol. 54, no. 6/7, pp. 477–491, Jun./Jul 2007.

[2] S. G. J. Aarninkhof and R. A. Holman, "Monitoring the nearshore with video," *Backscatter*, vol. 10, no. 2, pp. 8–11, 1999.

[3] H. F. Stockdon and R. A. Holman, "Estimation of wave phase speed and nearshore bathymetry from video imagery," *J. Geophys. Res.—Oceans*, vol. 105, no. C9, pp. 22 015–22 033, Sep. 15, 2000.

[4] K. T. Holland, "Application of the linear dispersion relation with respect to depth inversion and remotely sensed imagery," *IEEE Trans. Geosci. Remote Sens.*, vol. 39, no. 9, pp. 2060–2072, Sep. 2001.

[5] T. C. Lippmann and R. A. Holman, "Quantification of sand bar morphology: A video technique based on wave dissipation," *J. Geophys. Res.*, vol. 94, no. C1, pp. 995–1011, 1989.

[6] S. G. J. Aarninkhof, B. G. Ruessink, and J. A. Roelvink, "Nearshore subtidal bathymetry from time-exposure video images," *J. Geophys. Res.*, vol. 110, no. C6, p. C06 011, 2005. DOI:10.1029/2004JC002791.

[7] S. G. J. Aarninkhof and B. G. Ruessink, "Video observations and model predictions of depth-induced wave dissipation," *IEEE Trans. Geosci. Remote Sens.*, vol. 42, no. 11, pp. 2612–2622, Nov. 2004.

[8] N. G. Plant and R. A. Holman, "Intertidal beach profile estimation using video images," *Mar. Geol.*, vol. 140, no. 1, pp. 1–24, Jul. 1997.

[9] S. G. J. Aarninkhof, I. L. Turner, T. D. T. Dronkers, M. Caljouw, and L. Nipius, "A video-based technique for mapping intertidal beach bathymetry," *Coast. Eng.*, vol. 49, no. 4, pp. 275–289, Oct. 2003.

[10] S. M. Adler-Golden, P. K. Acharya, A. Berk, M. W. Matthew, and D. Gorodetzky, "Remote bathymetry of the littoral zone from AVIRIS, LASH, and QuickBird imagery," *IEEE Trans. Geosci. Remote Sens.*, vol. 43, no. 2, pp. 337–347, Feb. 2005.

[11] D. R. Lyzenga, N. P. Malinas, and F. J. Tanis, "Multispectral bathymetry using a simple physically based algorithm," *IEEE Trans. Geosci. Remote Sens.*, vol. 44, no. 8, pp. 2251–2259, Aug. 2006.

[12] J. V. Toporkov, D. Perkovic, G. Farquharson, M. A. Sletten, and S. J. Frasier, "Sea surface velocity vector retrieval using dual-beam interferometry: First demonstration," *IEEE Trans. Geosci. Remote Sens.*, vol. 43, no. 11, pp. 2494–2502, Nov. 2005.

[13] J. P. Dugan, C. C. Piotrowski, and J. Z. Williams, "Water depth and surface current retrievals from airborne optical measurements of surface gravity wave dispersion," *J. Geophys. Res.*, vol. 106, no. C8, pp. 16 903–16 915, 2001.

[14] J. P. Dugan, H. H. Suzukawa, C. P. Forsyth, and M. S. Farber, "Ocean wave dispersion surface measured with airborne IR imaging system," *IEEE Trans. Geosci. Remote Sens.*, vol. 34, no. 5, pp. 1282–1284, Sep. 1996.

[15] C. C. Piotrowski and J. P. Dugan, "Accuracy of bathymetry and current retrievals from airborne optical time-series imaging of shoaling waves," *IEEE Trans. Geosci. Remote Sens.*, vol. 40, no. 12, pp. 2606–2618, Dec. 2002.

[16] T. C. Lippmann and R. A. Holman, "Phase speed and angle of breaking waves measured with video techniques," in *Coastal Sediments '91*, N. Kraus, Ed. New York: ASCE, 1991, pp. 542–556.

[17] K. T. Holland, J. A. Puleo, and T. N. Kooney, "Quantification of swash flows using video-based particle image velocimetry," *Coast. Eng.*, vol. 44, no. 2, pp. 65–77, Dec. 2001.

[18] P. S. Bell, "Shallow water bathymetry derived from an analysis of X-band marine radar images of waves," *Coast. Eng.*, vol. 37, no. 3/4, pp. 513–527, Aug. 1999.

[19] J. A. Puleo, G. Farquharson, S. J. Frasier, and K. T. Holland, "Comparison of optical and radar measurements of surf and swash zone velocity fields," *J. Geophys. Res.*, vol. 108, no. C3, p. 3100, 2003. DOI:10.1029/2002JC001483.

[20] P. A. Catálan and M. C. Haller, "Remote sensing of breaking wave phase speeds with application to non-linear depth inversions," *Coast. Eng.*, vol. 55, no. 1, pp. 93–111, Jan. 2008.

[21] B. Jahne, J. Klinke, and S. Waas, "Imaging of short ocean wind waves: A critical theoretical review," *J. Opt. Soc. Amer. A, Opt. Image Sci.*, vol. 11, no. 8, pp. 2197–2209, Aug. 1994.

[22] C. M. Senet, J. Seemann, and F. Ziemer, "The near-surface current velocity determined from image sequences of the sea surface," *IEEE Trans. Geosci. Remote Sens.*, vol. 39, no. 3, pp. 492–505, Mar. 2001.

[23] C. G. Gelpi, B. C. Schuraytz, and M. E. Husman, "Ocean wave height spectra computed from high-altitude, optical, infrared images," *J. Geophys. Res.*, vol. 106, no. C12, pp. 31 403–31 413, 2001.

[24] W. Menke, *Geophysical Data Analysis: Discrete Inverse Theory*. New York: Academic, 1989.

[25] W. Munk, P. Worcester, and C. Wunsch, *Ocean Acoustic Tomography*. Cambridge, U.K.: Cambridge Univ. Press, 1995.

[26] S. Takashima, H. Asanuma, and H. Niitsuma, "A water flowmeter using dual fiber Bragg grating sensors and cross-correlation technique," *Sens. Actuators A, Phys.*, vol. 116, no. 1, pp. 66–74, 2004.

[27] S. Stramaglia, A. Refice, and L. Guerriero, "Statistical mechanics approach to the phase unwrapping problem," *Phys. A*, vol. 276, no. 3, pp. 521–534, Feb. 2000.

[28] T. H. C. Herbers, S. Elgar, and R. T. Guza, "Generation and propagation of infragravity waves," *J. Geophys. Res.*, vol. 100, no. C12, pp. 24 863–24 872, 1995.

[29] J. M. Oltman-Shay and R. T. Guza, "A data-adaptive ocean wave directional-spectrum estimator for pitch and roll type measurements," *J. Phys. Oceanogr.*, vol. 14, no. 11, pp. 1800–1810, Nov. 1984.

[30] M. A. Merrifield and R. T. Guza, "Detecting propagating signals with complex empirical orthogonal functions: A cautionary note," *J. Phys. Oceanogr.*, vol. 20, no. 10, pp. 1628–1633, Oct. 1990.

[31] W. H. Press, S. A. Teukolsky, W. T. Vetterling, and B. P. Flannery, *Numerical Recipes in C: The Art of Scientific Computing*, 2nd ed. Cambridge, U.K.: Cambridge Univ. Press, 1992.

[32] W. A. Birkemeier and C. Mason, "The CRAB: A unique nearshore surveying vehicle," *J. Surv. Eng.*, vol. 110, no. 1, pp. 1–7, 1984.

[33] C. E. Long and J. M. Oltman-Shay, "Directional characteristics of waves in shallow water," Coastal Eng. Res. Center, Field Res. Facility, U.S. Army Eng. Waterways Experiment Station, Vicksburg, MS, Tech. Rep. CERC-91, 1991.

Nathaniel G. Plant received the B.S. degree in earth sciences in 1989 and the M.S. degree in 1990 from the University of California, Santa Cruz, and the Ph.D. degree in oceanography from Oregon State University, Corvallis, in 1998.

He was an Oceanographer with the Naval Research Laboratory, Stennis Space Center, MS, from 2002 to 2007 and is currently an Oceanographer with the U.S. Geological Survey, St. Petersburg, FL. His research interests include studies of coastal processes and morphological evolution and prediction using both direct and remote sensing methods.

K. Todd Holland received the B.S. degree from Duke University, Durham, NC, in 1986 and the M.S. and Ph.D. degrees in oceanography from Oregon State University, Corvallis, in 1992 and 1995, respectively.

Since 1995, he has been an Oceanographer with the Naval Research Laboratory, Stennis Space Center, MS. He is a leading expert in the application of remote sensing technologies to the study of nearshore processes, particularly with respect to the use of motion imagery. He is currently developing new innovative techniques to characterize coastal areas using camera systems on small aerial vehicles.

Merrick C. Haller received the B.S. degree from Purdue University, West Lafayette, IN, in 1993, and the M.C.E. and Ph.D. degrees in civil engineering from the University of Delaware, Newark, in 1996 and 1999, respectively.

He currently holds joint appointments as an Assistant Professor in the School of Civil and Construction Engineering and the College of Oceanic and Atmospheric Sciences, Oregon State University, Corvallis. He has also worked as a Research Engineer with Veridian Systems Division and the University of Michigan, Ann Arbor. His present research interests include multisensor remote sensing of the nearshore ocean, wave breaking, rip currents, and wave–current interactions.

AUTHOR QUERIES

AUTHOR PLEASE ANSWER ALL QUERIES

ATTN: If you are paying to have all or some of your figures appear in color in the print issue, it is very important that you fill out and submit a copy of the IEEE Page Charge & Reprint Form along with your proof corrections. This form is available from the same URL where these page proofs were downloaded from. Thank you.

AQ1 = Rephrased. Edits correct?
AQ2 = Edits correct?
AQ3 = Ability of?
AQ4 = Lone left parenthesis was deleted. Original meaning preserved?
AQ5 = Added "respectively." Edits okay?
AQ6 = Several changes done. Original meaning preserved?
AQ7 = Please change figure labels to distinguish one from the other.

END OF ALL QUERIES

Ocean Wavenumber Estimation From Wave-Resolving Time Series Imagery

Nathaniel G. Plant, K. Todd Holland, and Merrick C. Haller

***Abstract*—We review several approaches that have been used to estimate ocean surface gravity wavenumbers from wave-resolving remotely sensed image sequences. Two fundamentally different approaches that utilize these data exist. A power spectral density approach identifies wavenumbers where image intensity variance is maximized. Alternatively, a cross-spectral correlation approach identifies wavenumbers where intensity coherence is maximized. We develop a solution to the latter approach based on a tomographic analysis that utilizes a nonlinear inverse method. The solution is tolerant to noise and other forms of sampling deficiency and can be applied to arbitrary sampling patterns, as well as to full-frame imagery. The solution includes error predictions that can be used for data retrieval quality control and for evaluating sample designs. A quantitative analysis of the intrinsic resolution of the method indicates that the cross-spectral correlation fitting improves resolution by a factor of about ten times as compared to the power spectral density fitting approach. The resolution analysis also provides a rule of thumb for nearshore bathymetry retrievals—short-scale cross-shore patterns may be resolved if they are about ten times longer than the average water depth over the pattern. This guidance can be applied to sample design to constrain both the sensor array (image resolution) and the analysis array (tomographic resolution).**

***Index Terms*—Adaptive signal processing, image processing, sea floor, sea surface, wavelength measurement.**

I. Introduction

Increasingly, observations of coastal processes are required over wide areas and at high spatial and temporal resolutions. In particular, recent modeling advances enable the simulation of wave parameters and wave-driven flows at resolutions as fine as a few meters. These model predictions require initial and boundary conditions, and because model results are often very sensitive to the details of the water depths, the bathymetry is an important boundary condition. In addition, the bathymetry may evolve significantly in several hours during storms or over longer time periods under more quiescent conditions. Therefore, providing models with up-to-date bathymetry is required to achieve accurate predictions. Furthermore, continuous bathymetric observations are essential in understanding the overall sediment and morphologic dynamics in coastal regions. As these observations are required both over large spatial regions and continuously in time, direct surveying methods are not up to this challenge, and remote sensing methods are required.

Shore-based remote sensing platforms can provide a continuous data stream that is also synoptic, typically spanning the region from the shoreline out to intermediate depths. For example, video camera stations are a numerous and well-established data source [1], [2]. With these data, it is possible to see the kinematic interaction of the incident wave field with the bathymetry (i.e., wave shoaling and refraction); hence, this information can be used to obtain estimates of bathymetry [3], [4]. An alternative approach for estimating bathymetry that utilizes time-averaged estimates of dissipation from remote sensing data [5]–[7] can only be applied in the surf zone and at the shoreline [8], [9]. It is possible to estimate bathymetry using other remote sensing approaches, such as multispectral or hyperspectral analysis [10], [11], which are typically deployed from aircraft.

Approaches to bathymetry estimation that are based on wave kinematics utilize the depth dependence of the wave speed or, equivalently, the wavelength and frequency, since $c = f/k$, where c is the wave phase speed, f is the wave frequency, and k is the wavenumber $= 1/L$, in which L is the wavelength. Overall, this approach requires image sequences, or time series of intensity at discretely sampled locations, that adequately resolve the wave motions. This situation differs from typical applications that use airborne or space-borne platforms, as those systems do not have long-enough dwell time to temporally resolve the surface waves but may be able to resolve the slowly varying current field [12].

The underlying methodology to solve this surface wave kinematics estimation problem has taken a number of different forms. These include finding the frequency and wavenumbers where spectral energy is a maximum [13]–[15], estimating the wavelength directly from a cross-shore-oriented pixel array at particular frequencies [3], estimating the time delay between a pair of image locations [16], and estimating spatial translations of the image field (the so-called particle image velocimetry) from sequential image pairs [17]. Once the wave speeds (or wavelengths) have been estimated, the data can be used to estimate depth via a wave dispersion relationship. This last step requires an inverse model solution that solves for a depth that minimizes differences between the predicted speed (from the dispersion relationship) and the estimated speed (from the imagery).

The diverse methodologies listed above are similar in that most are designed to extract estimates of wavenumber

Manuscript received January 25, 2008; revised xxxx. This work was supported by the Office of Naval Research through the base funding program element under Contract 0602435N.

N. G. Plant was with the Naval Research Laboratory, Stennis Space Center, MS 39529 USA. He is now with the U.S. Geological Survey, Florida Integrated Science Center, St. Petersburg, FL 33701 USA (e-mail: nplant@usgs.gov).

K. T. Holland is with the Naval Research Laboratory, Stennis Space Center, MS 39529 USA (e-mail: tholland@nrlssc.navy.mil).

M. C. Haller is with the School of Civil and Construction Engineering, Corvallis, OR 97331 USA (e-mail: hallerm@engr.orst.edu).

Color versions of one or more of the figures in this paper are available online at http://ieeexplore.ieee.org.

Digital Object Identifier 10.1109/TGRS.2008.919821

components at discrete frequencies from the imagery. However, it is not clear how well each method performs in a wide range of environments, including the laboratory, open water (where wavenumber variations that are controlled by currents may be important), open coasts (i.e., long straight beaches), and enclosed coasts (which have inlets and strong wave–current interactions). In addition, it is not clear how well each method can be applied to other imaging modalities, such as microwave radar [18], [19]. Therefore, the objective of this paper is to quantify the sensitivity of wavenumber estimation methods to variations in the sample design (e.g., spatial and temporal resolutions) and signal-to-noise ratios of the imaging system. To understand the situation, we will decouple the wavenumber estimation problem from that of estimating water depth. To this end, we define the problem, and we derive a formal inverse model that solves for the unknown spatially variable wavenumbers from image sequences (or intensity time series from a subset of image pixels). We evaluate the suitability of various sampling scenarios, including 1- and 2-D spatial AQ3 arrays. In addition, we evaluate the abilityto predict the errors of the wavenumber estimates. Error predictions are essential for quantitative quality control and impact the results of subsequent bathymetry estimations as well as field evaluations of, for example, wave dispersion models [4], [20].

This paper is organized as follows. In Section II, we describe the general problem of wave phase speed estimation and its equivalent wavenumber estimation problem, and we derive an inverse model for estimating spatially varying wavenumbers. In Section III, we evaluate the skill of the newly developed method using both synthetic and real-world data sets applied to both 1- and 2-D spatial domains. In Section IV, we discuss the similarity and differences between existing wavenumber estimation approaches, and we quantify the theoretical constraints on the spatial resolution of wavenumber and bathymetry estimates. Section V summarizes the important results, including the following: 1) that the proposed method provides improved spatial resolution and quantitative error predictions and 2) that it is well suited to solve the bathymetry inversion problem.

II. Theory

We assume that georeferenced image sequences exhibiting intensity modulations attributable to surface gravity waves are available and that their sampling rate is sufficient to resolve a significant portion of the gravity wave spectrum. The imagery can be expressed as $I(x_i, y_i, t)$, where x_i, y_i is the spatial coordinate of the ith image pixel, and t represents discrete sampling times. At frequencies of interest, we wish to characterize the spatial variation of the wave field, including the changes in wavelength and direction that occur in nearshore areas due to shoaling and refraction.

Our first objective is to describe an efficient and accurate method of calculating estimates of c (or, equivalently, k). We will make some additional simplifying assumptions. For example, many details regarding the sensor imaging mechanisms, such as light absorption, reflection, and scattering, are ignored [21]. Variance introduced at sum/difference frequencies and wavenumbers via wave nonlinearity is also ignored [22]. The (spatially) unresolved portion of the image signal, corresponding to water waves that are shorter than the Nyquist wavelength of the image samples, is not treated in detail other than to assume that it will appear as white noise. This aliased component can be resolved [15], [23], but this is probably only required if we were attempting to reconstruct the details of the time-varying sea surface. Instead, our focus is on extracting the resolvable spatial variability of the wavenumber vector field. Finally, we assume that this variability can be described by a finite number of modes. For example, a particularly egregious assumption will be that the wave field at a single frequency is locally well represented by a single wavelength and direction. Our approach tests this particular hypothesis with a quantitative model so that violations can be identified.

A. Time Delay Problem Definition

We assume that time delay information is available from the spatially separated pixels such that an intensity time series at one location can be predicted from observations at another location, i.e.,

$$I(x_i, y_i, t) = g_{i,j,n} I(x_j, y_j, t + \Delta t_{i,j,n}) + e_{i,j,n}(t) \tag{1a}$$

where the time lag $\Delta t_{i,j,n}$ maximizes the correlation or min- AQ4 imizes the variance of the error $e_{i,j,n}$ between observations at sample locations x_i, y_i and x_j, y_j due to the nth wave component. The parameter $g_{i,j,n}$ is a tunable correlation coefficient. In one spatial dimension (e.g., normal to the shoreline), the time lag is related to the wave properties as

$$\begin{aligned}\Delta t_{i,j,n} &= \int_{x_i}^{x_j} \frac{\cos(\alpha_n[x])}{c_n[x]} dx \\ &= \int_{x_i}^{x_j} \frac{\cos(\alpha_n[x])\, k_n[x]}{f_n} dx\end{aligned} \tag{1b}$$

where α_n is the direction of the nth wave component (e.g., it corresponds to a discrete frequency and wavenumber f_n, k_n, respectively), and c_n is the celerity of that wave component. AQ5 The cosine inside the integral indicates that the analysis only resolves the wave component in the shore-normal direction. This equation is the basis for any tomographic analysis applied to physical properties of the Earth [24], including the speed of sound waves in the ocean [25].

The wave field can be described in a discrete spatial domain with spacing Δx. The discrete time delay equation becomes

$$\begin{aligned}\Delta t_{i,j,n} &= \Delta x \sum_{m=1}^{M} D_{i,j,m} \frac{\cos(\alpha_n[x_m])}{c_n[x_m]} \\ &= \Delta x \sum_{m=1}^{M} D_{i,j,m} \frac{\cos(\alpha_n[x_m])}{f_n} k_n[x_m]\end{aligned} \tag{2}$$

where the matrix D is a design matrix defined on both the sample domain x_i, x_j and the estimation domain described by location x_m. (We will refer to the estimation domain as the tomographic domain to maintain that analogy.) The design matrix describes how each observation contributes information to the estimate of the unknown model parameters $\alpha_{n,m}$ and $k_{n,m}$. In 1-D, elements of D are equal to unity between two sensors and are zero elsewhere. Smoothness constraints can be implemented through filtering of D such that sharp changes in the estimated celerity are not permitted.

Clearly, in this form, the time delay equation is linear with respect to the unknown wavenumbers. The number of observations required to solve the problem must be at least equal to the number of elements M in the tomographic domain. Furthermore, the spatial distribution of the observations is important. For instance, an element in the center of an array of observations will have many contributions, whereas elements at the ends of the array will have fewer contributions. Thus, while the resolution of x_m is arbitrary, the resolvable scales of intensity variance depend on the data sampling resolution.

To utilize the time delay equation with remotely sensed imagery, one must estimate the time lag Δt associated with the propagation of the visible wave signal. The time lag will differ for all sensor pairs. This requires some sort of a search for the Δt that corresponds to a maximum in the cross correlation function $r_{i,j}$, as given by

$$r_{i,j}(\Delta t) = W(\Delta t)^* \langle I(x_i, t) I(x_j, t + \Delta t)\rangle \tag{3}$$

where W is a bandpassed filter that is convolved against the cross correlation, and the angle brackets indicate an ensemble average over all observation times. This method has recently been used, for instance, in the estimation of flow speeds with fiber optic sensors [26]. At this stage, the estimation of the time delays typically requires a nonlinear search algorithm; therefore, the linearized version of the time delay equation does not avoid a nonlinear estimation step.

B. Phase Delay Problem Definition

Since it is natural to work with wave processes in the frequency domain, an alternative approach is to apply a discrete Fourier transform to the observations and rewrite the time delay as a phase delay by computing the cross-spectral correlation between two sensors as follows:

$$\begin{aligned} C_{i,j,f}^{\mathrm{OBS}} &= \left\langle \tilde{I}(x_i, f)\tilde{I}^*(x_j, f)\right\rangle \\ &= \gamma_{i,j,f} \exp\{\sqrt{-1}\Phi_{i,j,f}\} \end{aligned} \tag{4}$$

where the tilde indicates the Fourier transform, the asterisk indicates the complex conjugate, angle brackets indicate ensemble or band averaging, γ is the coherence, and Φ is the phase shift between two sample locations x_i and x_j for a particular frequency. Since the phase shift between two sensors is $\Phi_{i,j,f} = f\Delta t_{i,j,f}$, replace Δt with the right-hand side of (2), and insert the resulting expression for Φ into (4) to get a model for the cross-spectral correlation, which is described as follows:

$$C_{i,j,f}^{\mathrm{MODEL}} = \exp\left\{2\pi\Delta x\sqrt{-1}\sum_{m=1}^{M} D_{i,j,m} k_{m,f}\cos(\alpha_{m,f})\right\}. \tag{5}$$

While the time delay equation is linear in the cross-shore wavenumber $k_{m,f}\cos(\alpha_{m,f})$, the cross-spectral correlation equation is a nonlinear function of the wavenumber.

An apparent advantage of the spectral formulation is that the problem of filtering the time series within particular frequency bands is accomplished via Fourier transform, and the nonlinear problem of identifying time delays in the observations is avoided. A disadvantage of the Fourier transform approach is a requirement for sufficient sample duration to resolve the frequencies of interest. This disadvantage is mitigated by the use of coherence to identify robustness of the analysis. A further disadvantage is that a phase ambiguity exists such that $\Phi_{\mathrm{estimate}} = \Phi_{\mathrm{true}} - (2\pi b)$, where b is the phase ambiguity, and Φ_{estimate} lies on the interval $(-\pi, \pi)$. Thus, sample locations that are separated by more than a wavelength are susceptible to aliasing when the phase ambiguity is unknown. (Piotrowski and Dugan [15] deal with this by guessing at the ambiguities.) This problem is well known and has received much recent attention in applications of synthetic aperture radar interferometry. The solutions for cases with potentially large phase ambiguities may be solved via simulated annealing [27]. In the present approach, we will assume that there are a sufficient number of sensor separations that suffer no phase ambiguity—given a decent initial guess of the true wavenumbers, these sensor separations can be identified *a priori*. A data-adaptive identification method is explained in Section II-C-3.

C. Wavenumber Estimation Solution Methods

Previous approaches to estimating wavenumbers (and directions) at a particular frequency contain different mixtures of local and nonlocal solutions to the problem. For instance, the approach of Piotrowski and Dugan [15] assumes locally horizontal bathymetry (implying spatially constant wavenumber magnitude and wave direction over an analysis region) and calculates the image intensity spectrum as a function of two wavenumber components and frequency via Fourier transforms. This spatially homogeneous spectrum assumption is applied over a large number of nearby sample locations (commonly a 256 × 256 patch of pixels, with a typical resolution of 1 $\mathrm{m}^2\mathrm{pixel}^{-1}$). For all wavenumber components, a frequency of maximum spectral density is identified. This approach does not directly utilize correlations across regions where the wavenumber is changing (in the shoaling region), which are explicitly contained in the formulation given by (2). There are other approaches used to analyze spectral energy distribution of wavenumber (e.g., [28] and [29]), but these also assume spatial homogeneity.

We seek to avoid the restriction of spatial homogeneity because, for example, it is commonly not applicable in nearshore areas where bathymetry and currents can induce rapid wavenumber variations over short distances and where a higher resolution is required. Hence, we turn our attention to solution methods that fully utilize the available spatial correlation information. These allow a highly resolved spatially variable wavenumber field. Furthermore, we will focus on the spectral approach based on (4) rather than the time-domain approach that would be based on (2).

1) Single-Mode Analysis: In general, at a single frequency, numerous wave trains, each with different directions, could contribute to the cross-spectral correlation estimate defined by (4). Thus, the original tomographic equation relating time delay to wave speed is inherently a stochastic problem, with each wave train contributing to and blurring the best-fit speeds and the corresponding time delays. One possible approach for separation of the various contributing wave trains is to decompose the cross-spectral correlation into the most coherent modes as follows:

$$C_{i,j,f}^{\mathrm{OBS}} = \sum_{q=1}^{Q} P_{i,q,f} \Gamma_{q,f} P_{j,q,f}^{*} \tag{6}$$

where $\Gamma_{q,f}$ is the $Q \times Q$ diagonal matrix with eigenvalues of $C_{i,j,f}^{\mathrm{OBS}}$, and $P_{i,q,f}$ are the corresponding eigenvectors. In their approach to estimating bathymetry from video imagery this way, Stockdon and Holman [3] selected the first (dominant) eigenmode to approximate the cross-spectral matrix at a single dominant frequency. The magnitude of the eigenvector at each location x_i indicates its contribution to the total correlation, and the spatial phase differences are described by the phase of the eigenvector. To extract wavenumber information, which is related to the gradient of the phase, Stockdon and Holman [3] unwrapped the phases of P and estimated the local gradient of the potentially noisy phase estimates, e.g.,

$$\hat{k}_{i,f} = \frac{1}{2\pi} \frac{\hat{\phi}_{i+1,1,f} - \hat{\phi}_{i-1,1,f}}{(x_{i+1} - x_{i-1})}. \tag{7}$$

This estimate is the cross-shore component of the dominant wavenumber, and the full wavenumber requires an estimate of the alongshore component, which they obtained from a different analysis approach and was assumed constant across the domain.

Although this method is computationally efficient, it suffers several disadvantages. First, using only the first eigenmode requires significant coherence across the entire domain. Typically, the center of the domain will dominate the first mode [30]. Thus, the phase estimates at the offshore and onshore ends of the array and at the location of wave breaking (where coherence and phase are disrupted by changes in the imaging mechanism for optical data) may be poorly estimated. Second, phase errors due to observation noise or phase ambiguity are difficult to estimate, which is problematic because error predictions are essential for assessing the value of the extracted data. A potentially devastating situation is that of an array with very dense samples such that the denominator of (7) approaches zero and the estimate primarily amplifies measurement errors, rather than identifying the slowly varying wavenumber. Finally, there is potentially useful information at multiple wave frequencies in addition to that at the "dominant" frequency. The identification of a "dominant" frequency involves tradeoffs between signal strength, spatial coherence, and spatial resolution. These attributes are not necessarily the maximum at all spatial locations at the "dominant" frequency. As we will show, there are several advantages utilizing information from multiple frequencies.

2) Nonlinear Inversion Method: Since wavenumber is nonlinearly related to the cross-spectral correlation, a typical nonlinear inversion method, such as Levenberg–Marquardt (LM) [31], can be used. The objective is to minimize the weighted squared difference between successive estimates of the modeled cross-spectral correlation when compared to the observations, i.e.,

$$\Delta C_{i,j,f}^{\tau} = \left\{ \gamma_{i,j,f} C_{i,j,f}^{\mathrm{MODEL},\tau} - C_{i,j,f}^{\mathrm{OBS}} \right\} \tag{8}$$

where, at each iteration τ, the model–observation mismatch is weighted by the observed coherence. For the 1-D case, we cannot estimate the wave angle and, therefore, will only obtain estimates of the cross-shore component of the wavenumber. However, extension to two horizontal dimensions is straightforward (see Section III-C), given 2-D image sequences. Linearized models for the wavenumbers on the tomographic domain are solved iteratively as follows:

$$\begin{aligned} k_{f,m}^{\tau+1} &= k_{f,m}^{\tau} + \Delta k_{f,m}^{\tau} \\ \Delta k_{f,m}^{\tau} &= \left([R^{\tau}]^{T} R^{\tau} \right)^{-1} [R^{\tau}]^{T} \Delta C_{i,j,f}^{\tau} \\ R^{\tau} &= R_{i,j,m,f}^{\tau} \\ &= \gamma_{i,j,f} \sqrt{-1} D_{i,j,m} C_{i,j,f}^{\mathrm{MODEL},\tau} \Delta x. \end{aligned} \tag{9}$$

The model–observation mismatch is ordered as a column vector, with each element corresponding to a particular $i-j$ pair of observation locations. The matrix R describes the sensitivity of the cross-spectral correlation to the variation in each wavenumber in the tomographic domain. Thus, each column of R corresponds to the elements in the tomographic domain x_m, and each row corresponds to a $x_i - x_j$ spatial separation pair. It is possible to efficiently compute R by evaluating $C^{\mathrm{MODEL},\tau}$ at the observation locations. In the case where the predicted wavenumber updates $\Delta k_{f,m}^{\tau}$ do not converge (according to an *a priori* tolerance), the LM method diagonalizes R such that the minimization method is equivalent to gradient descent search.

Error predictions for the wavenumber estimates are computed as

$$(\varepsilon_f^{\tau})^2 = \mathrm{diag}\left([R^{\tau}]^{T} [R^{\tau}] \right)^{-1} \left(\left[\Delta C_f^{\tau} \right]^{T} \left[\Delta C_f^{\tau} \right] \right) / \nu \tag{10}$$

where the degrees of freedom ν equals the sum of the coherences. This error prediction assumes that the errors in the wavenumber updates are normally distributed, and that the data are independent. The latter assumption is certainly not true, since data from a single observation location contributes to many observation pairs in the cross-spectral correlation estimate. However, the error predictions should provide good estimates of the relative error at different locations. Those locations with strong sample support $(D > 0, \gamma > 0)$ and strong sensitivity $(d/dk|C^{\mathrm{MODEL}}| > 0)$ will have the lowest error.

The nonlinear inverse method satisfies some important criteria for providing robust wavenumber estimates. First, it allows a spatially variable solution that can be applied to all available frequencies. Second, error estimates that reflect the sample design, the signal coherence, and the desired solution resolution are easily computed for use in assessing data quality. We therefore suggest this to be the most appropriate approach to wavenumber estimation in nearshore settings. The primary drawback to implementation of the method is additional computational complexity. However, this drawback can be handled using existing computational capabilities, including efficient matrix operations, multiprocessor computers, and ever-increasing memory.

3) Implementation Issues: Some final implementation issues are addressed here. They encompass choices that must be made about the analysis domain, which can have very different and typically coarser resolution properties compared to the image data. The tomographic resolution is a free parameter for any application of this methodology. The cost of high resolution is a larger sample design matrix D and a larger sensitivity matrix R. Both must be stored in the computer memory, and the latter must be squared and inverted. The cost of low resolution is an inaccurate representation of the spatial variations of the wavenumber. To balance these two costs, we chose to represent the wavenumber estimate with basis functions such that

$$k_i = \sum_{m=1}^{M} a_{i,m} k_m \tag{11}$$

where a k_m basis set is defined on a relative coarse domain, and $a_{i,m}$ represents smoothing weights used to project the basis set to an arbitrary location x_i. The smoothing weights can be any filter function. We used a Hanning filter

$$\begin{aligned} a(\delta_{i,m}) &= \{1 - \cos(0.5\pi[1 + \delta_{i,m}])\}^2, \qquad \text{if } r_{i,m} < 1 \\ \delta_{i,m} &= |x_i - x_m| L_x^{-1} \end{aligned} \tag{12}$$

where L_x is a smoothing lengths scale. A smooth solution requires $L_x > \Delta x_m$ (where Δx_m is the tomographic domain resolution). The sample design matrix must be modified to include the spatial correlation imposed by the basis function

$$D_{i,j,m} = \sum_{i'=i}^{j} a_{i',m}. \tag{13}$$

Additionally, to impose continuity on estimates in regions where there might be large data gaps, the sensitivity matrix R used in (9) was augmented with the basis autocorrelation such that $R' = R + \mu Q$ and $Q = [a_{m,m'}]^T a_{m,m'}$, where $\mu = 0.1$ was used. This solution balances minimizing the cross-spectral correlation errors against errors due to spatially erratic results that are associated with unresolved scales of the solution.

While the coarse resolution (Δx_m) of the tomographic domain should be designed to adequately resolve the bathymetry, it does not adequately resolve the much shorter scale of the wave phase variations. Using x_m directly in (5) would lead to integration errors in the model for the cross-spectral correlations. To solve this problem, the coarsely defined and smoothly varying wavenumbers on the x_m domain were interpolated to a much finer grid spacing of 1 m, using (11). Phases were then integrated to each observation location on this fine grid using (5).

Phase ambiguity remains to be a problem. A particular phase difference at large spatial separations might result from the integration over a large number of short wavelengths, or integration over a fraction of a larger wavelength. Mismatches between the observed and predicted phase of the cross-spectral coherence at these large lags may not be very useful in indicating whether a wavenumber estimate should be locally increased or decreased to improve the fit to the observations. Since the LM method assumes small phase errors, the coherence can be artificially reduced at long lags by applying a Hanning window mask (12) with a length scale parameter that adaptively depended on the wavenumber estimate: $L_m^\tau = 1/k_{\max}^\tau$, where $k_{\max}$ is the maximum computed wavenumber in the domain. The mask was applied to the sensitivity as $R'_{i,j} = R_{i,j} a_{i,j}$ (i.e., an element-wise multiplication, not convolution). We found that this approach worked well for initial wavenumber guesses that were either too high or too low. In principle, as the estimate converges, more distant sensor pairs may be allowed to contribute to the solution by increasing the length scale of the mask.

Finally, the iterative estimation scheme requires an initial wavenumber estimate. We suggest generating an initial estimate using linear wave theory and an estimate of the water depths.

III. Applications

A. Synthetic Example

To evaluate the suggested wavenumber estimation approach, we applied it to a synthetic data set. Cross-spectral correlations [Figs. 1(a) and (b) and 2(a) and (b)]were computed for two frequencies (i.e., 0.1 and 0.2 Hz) using linear wave theory to construct wavenumber profiles from a planar depth profile [Figs. 1(c) and 2(c)]. Random errors were included in the cross-spectral correlation by adding 50% random noise to the "true" wavenumber profile [Figs. 1(d) and 2(d)] and summing the resulting phases over 100 realizations. This combination of noise level and number of realizations produced cross-spectral correlations with a realistic coherence decay with increasing sensor separation distances. The phases were sampled at location x_j, with spacing Δx of 5 m. The cross-spectral correlation phases are, by definition, zero along the diagonal (i.e., where the signal from location x_j is compared to itself) and are antisymmetric about the diagonal ($\Phi_{ij} = -\Phi_{ji}$). The simulation shows that the wavelength is longer offshore (phase differences change slowly with spatial lags) and is shorter nearshore. The low-frequency (longer) waves are better resolved (broader coherence and clearly periodic phase structure) than the high-frequency waves (narrow coherence, random phase structure at large spatial separations).

Wavenumber estimates and corresponding error predictions were obtained using the nonlinear inverse method on a tomographic domain with spacing $\Delta x_m = 20$ m. We performed several experiments, including using all of the data, removing some of the sample data in a patch located between 50 m $< x <$ 100 m, and initializing the iterative method with wavenumbers that were too large and too small. Fig. 3 shows the estimation results applied to both frequencies. The estimated wavenumbers

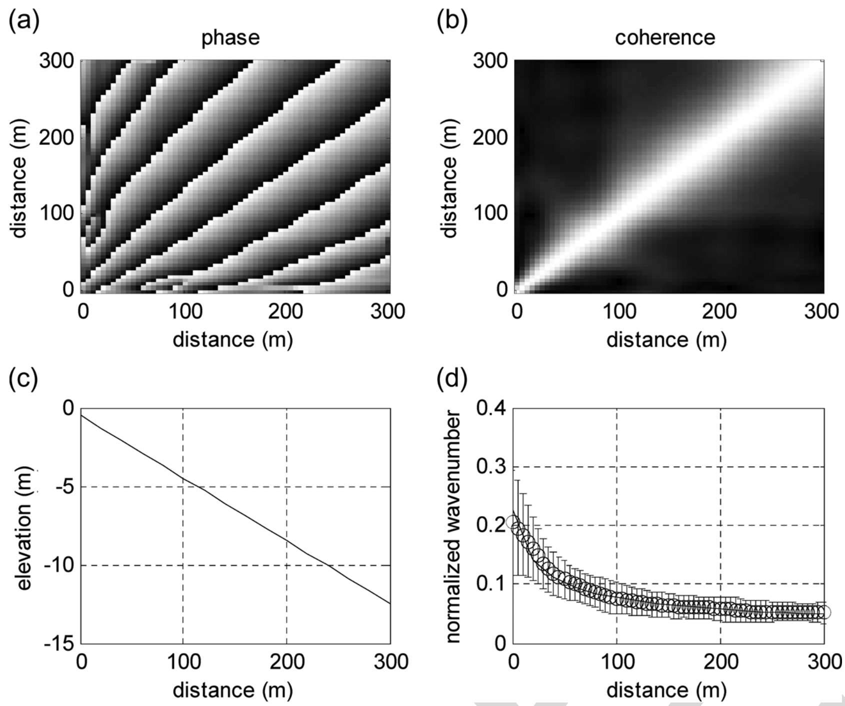

Fig. 1. Cross-spectral correlation (a) phase and (b) coherence for 0.1-Hz (10 s) wave propagation over (c) plane-sloping bathymetry. (d) Wavenumber samples were generated using linear wave theory plus a random variation. Error bars show one standard deviation. Wavenumbers are shown normalized by the sample spacing such that the Nyquist wavenumber occurs at a value of 0.5. Shading scale is (a) black $= -\pi$, white $= \pi$ and (b) black $= 0$, white $= 1$.

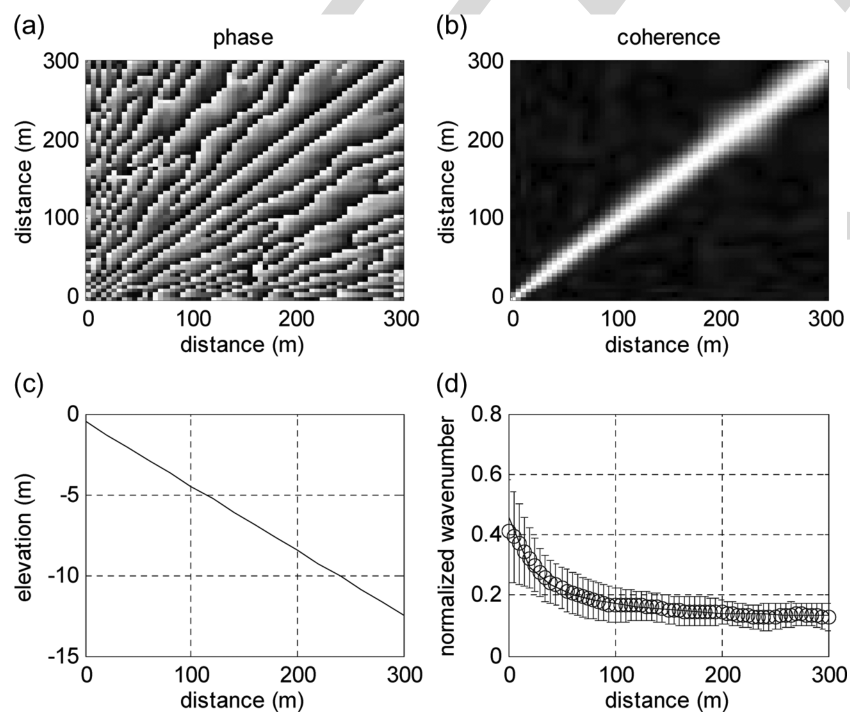

Fig. 2. Cross-spectral correlation phase and coherence for 0.2-Hz (5 s) wave propagation. Description of each panel is the same as in Fig. 1.

were very accurate at nearly all locations. At locations where the estimate was relatively inaccurate, such as near the location of the data gap, the error predictions (10) were also large. It is worth noting that the wavenumber estimate depends on the initial guess of the wavenumber in the region where data were missing. While such dependence on the initial guess is undesirable, the predicted errors correctly identify the region that is susceptible to the problem.

B. Field Data Example

We evaluated the nonlinear inversion method for wavenumber estimation using observations from a set of video cameras mounted on a tower at the U.S. Army Corps of Engineers Field Research Facility (FRF), Duck, NC. The cameras did not store full image frames (Fig. 4) during the study period, but instead, time series of intensity at a sparse set of spatial locations

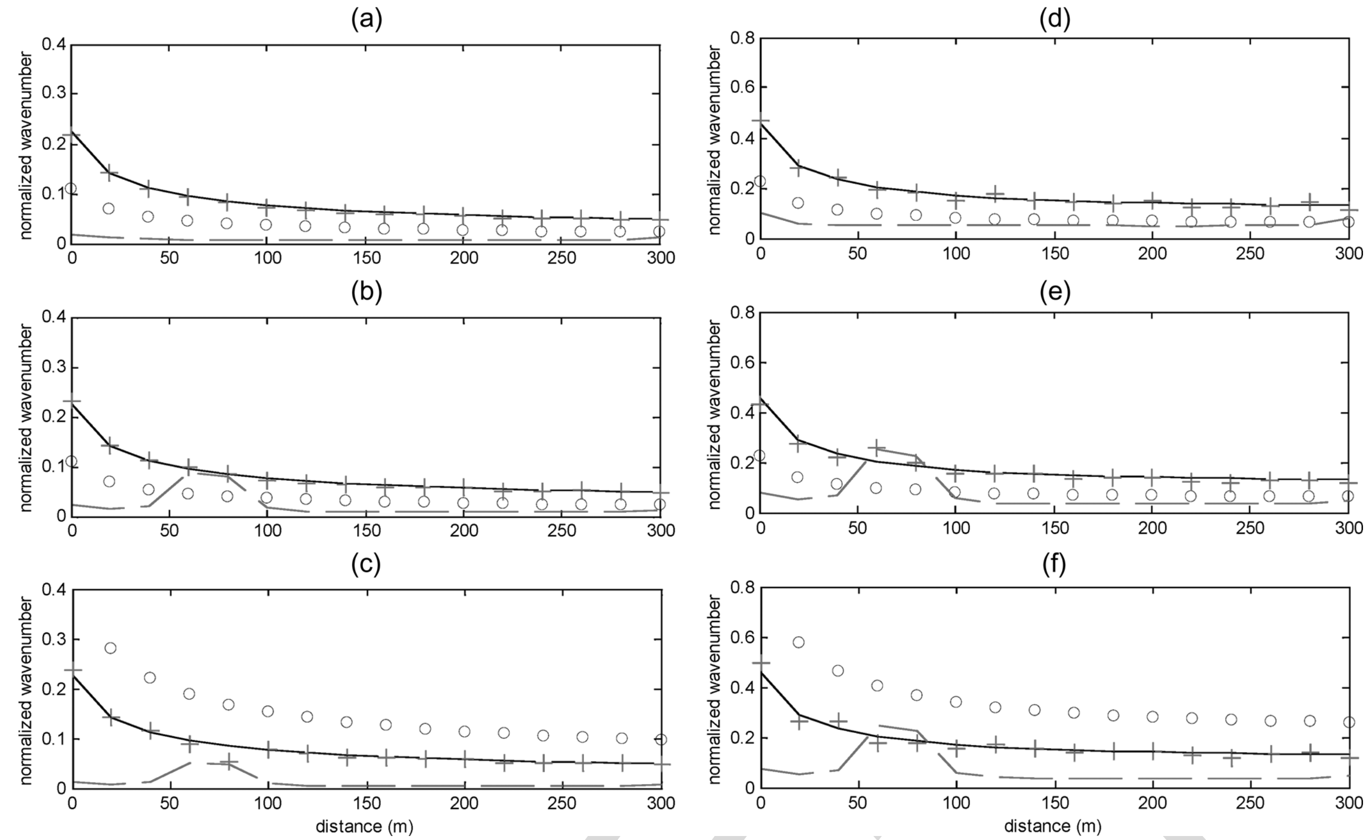

Fig. 3. Example wavenumber estimates using synthetic data for (a–c) a 10-s period and (d–f) a 5-s period. The estimation is started out with initial guess (circles) that is half the true value (a and d). The estimate $(+)$ is nearly identical to the true value (solid line). The rms error predictions (dashed line) are larger for the less well-resolved 5-s period data. In the second experiment (b and e), a 50-m patch of the observations was removed between $50 < x < 100$ m. In the third experiment (c and f), the initial guess is twice the true value.

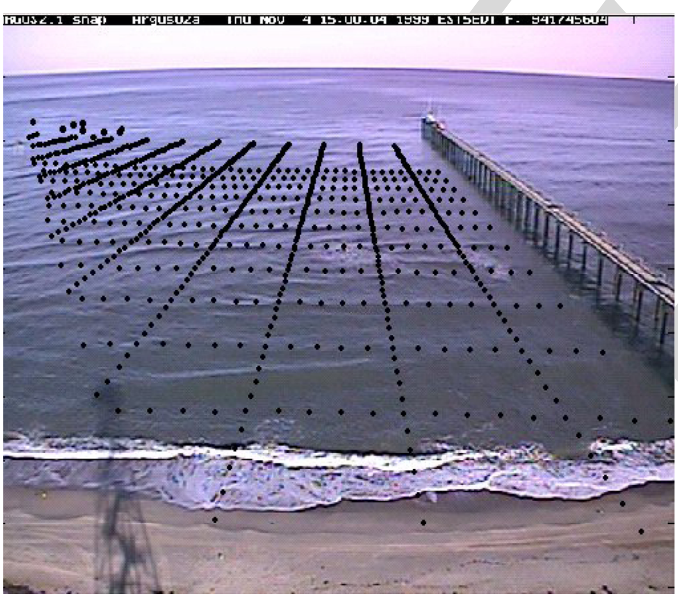

Fig. 4. Camera view of the Duck field site, showing the image time series sample locations (black dots). The camera orientation and distortion are used to map the data to georeferenced locations. The cameras are mounted on a tower, whose shadow on the beach provides a self-portrait.

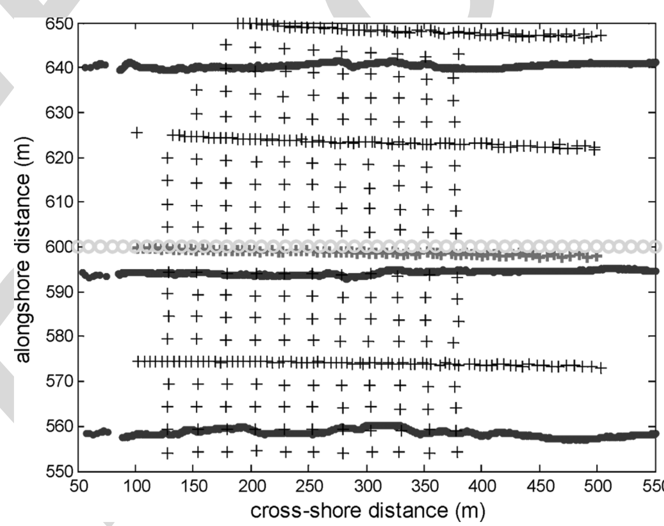

Fig. 5. Duck sampling pattern with the shoreline at the left near $x = 100$. Bathymetric survey locations are indicated by dots (very densely spaced in the cross-shore direction); image time series $(+)$ were sampled over the 2-D domain. The samples used in the 1-D analysis are indicated with bold symbols. Wavenumbers were estimated on a sparse tomography domain, which is indicated by circles (1-D case).

were retained for analysis (Fig. 5). This sampling scheme was implemented to balance data storage constraints against the requirements for resolving the important components of the incident wave field. With a cross-shore sample spacing of about 5 m, waves longer than 20 m (half the Nyquist wavenumber) should be well resolved. This corresponds to waves with a period longer than 6 s at a water depth of 1 m. At the Duck field site, the annual mean wave period is about 8 s, which means that a depth of 1 m, these waves have a 25-m wavelength

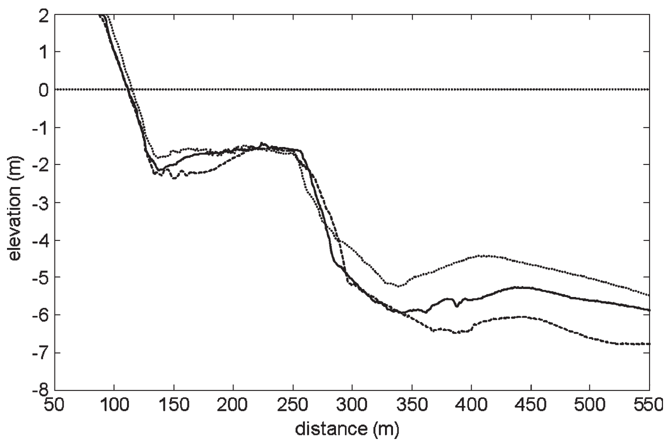

Fig. 6. Cross-shore bathymetry transect surveyed on November 4, 1999, at an alongshore location near 600 m (solid line), 560 m (long dash), and 640 m (short dash).

and are well resolved. With this array design, these waves are resolvable until water depths reach about 0.75 m. Thus, for this field site, and depending on tidal height, wavenumber estimates should be possible for the region offshore of about $x = 120$ m (Fig. 6).

As in the synthetic example, we chose a cross-shore resolution of $\Delta x_m = 20$ m for the tomographic domain and a corresponding smoothing scale of $L_x = 40$ m. At the FRF, ground-truth bathymetry data were obtained from a three-wheeled (10-m footprint) survey vehicle, called the Coastal Research Amphibious Buggy [32]. The ground-truth bathymetry along the 1-D cross-shore transect (Fig. 5, middle) that is used in this analysis is shown in Fig. 6. It includes a very steep swash zone (near $x = 120$ m), an inner sand bar ($x = 230$ m), and an outer sand bar ($x = 450$ m). While the remote sensing data extend from 100 m $< x <$ 500 m, we estimate the wavenumber both onshore and offshore of this extent. The error predictions should indicate the locations where robust wavenumber estimates are available.

Using the pixel array data collected on November 4, 1999, at approximately 20:00 GMT, the sample cross-spectral correlation (4) was computed at a series of frequencies ranging from 0.07 Hz (15-s wave period) to 0.23 Hz (4-s wave period). The record length was 68 min, and the sample interval was 0.5 s. The band-averaged frequency resolution was 0.03 Hz, with 136 nonoverlapping frequency samples used in each band. The phase and coherence are shown in Fig. 7 for each sample frequency. Only the lower portion of the symmetric correlation matrix was computed and stored. Spatial coherence, summed over all spatial separations, was highest at 0.167 Hz (6 s), followed by 0.10 Hz (10 s), and then 0.2 Hz (5 s) (Table I). We expect that these frequencies will yield accurate wavenumber estimates if the corresponding wavenumber structure is spatially well resolved. Note that the peak wave energy does not necessarily correspond to the peak coherence. In this case, the peak wave period based on sea surface height measured 8 m offshore was 8.9 s (0.11 Hz); the peak direction was 24° south of the shore normal; and the significant wave height was 0.5 m.

The nonlinear inverse estimation method was applied to the sample cross-spectral correlations at each frequency over the entire array. To initialize the iterative method, at each frequency, a linear dispersion model was used (assuming shore-normal wave incidence) to generate initial wavenumbers at each location x_m. We used a bathymetry with a constant depth of 1 m for the initial guess.

For the purpose of comparison, linear wave theory was used to compute the "true" wavenumber for each frequency.

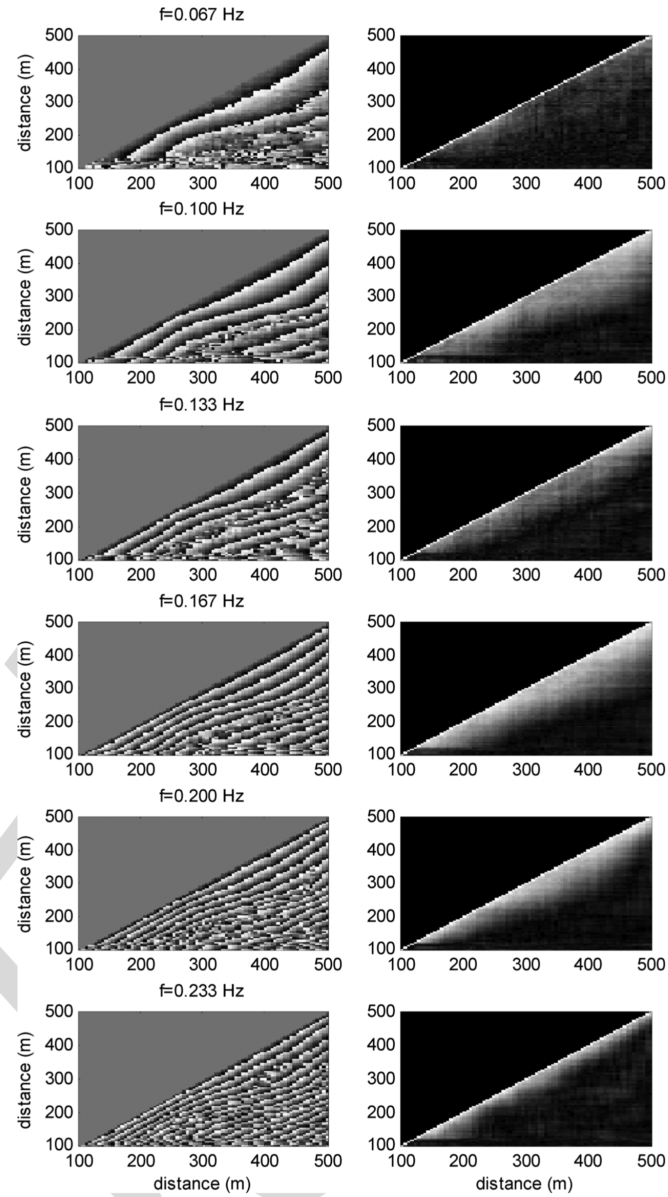

Fig. 7. (Left column) Phase and (Right column) coherence for individual frequencies determined from pixel array data (Duck, NC).

TABLE I
COHERENCE AND WAVENUMBER ERROR STATISTICS

Frequency (Hz)	Total Coherence	RMS wavenumber error (m^{-1})
0.067	609.051	0.020
0.100	999.266	0.026
0.133	748.390	0.034
0.167	1052.162	0.048
0.200	855.658	0.053
0.233	638.458	0.068

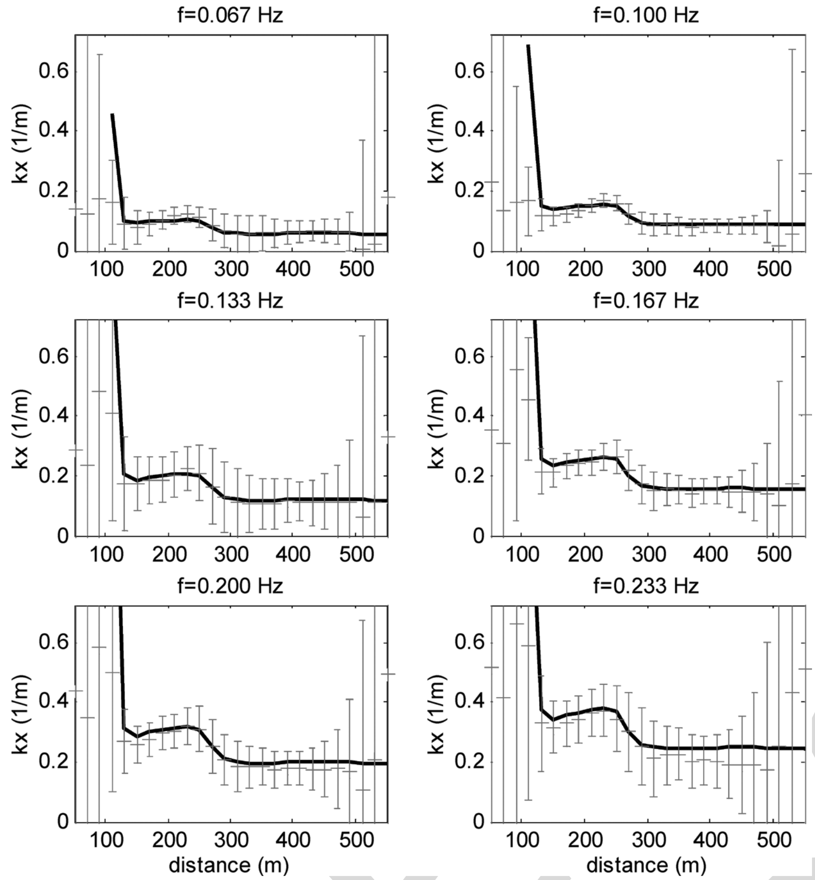

Fig. 8. Wavenumber estimates using Duck data. Error bars show the rms error prediction. Solid line shows linear wave theory prediction for each frequency.

The measured bathymetry and tide level at the time of the image collection was used. (We acknowledge that linear wave theory gives an imperfect ground-truth for parts of our analysis domain [20].) Fig. 8 shows the comparison of the "true" and estimated wavenumbers. The rms mismatch between the "true" and estimated wavenumbers was computed by using the predicted errors as weights. Thus, locations where the predicted errors (shown as error bars) were relatively high did not contribute as much to the rms error. The best estimates (Table I) were obtained for the lowest frequency (0.067 Hz, rms error 0.02 m^{-1}). This is a bit surprising, given the low coherence at this frequency. However, these waves are relatively long, and their spatial structure is well resolved by the sample design. The three frequencies with largest spatial coherence also had relatively low rms errors. Importantly, the spatial distribution of the predicted errors reflected the locations having high-quality data. Overall, the estimated wavenumbers were correlated to the "true" values with $r^2 = 0.96$ and a slope of 1.0 (Fig. 9).

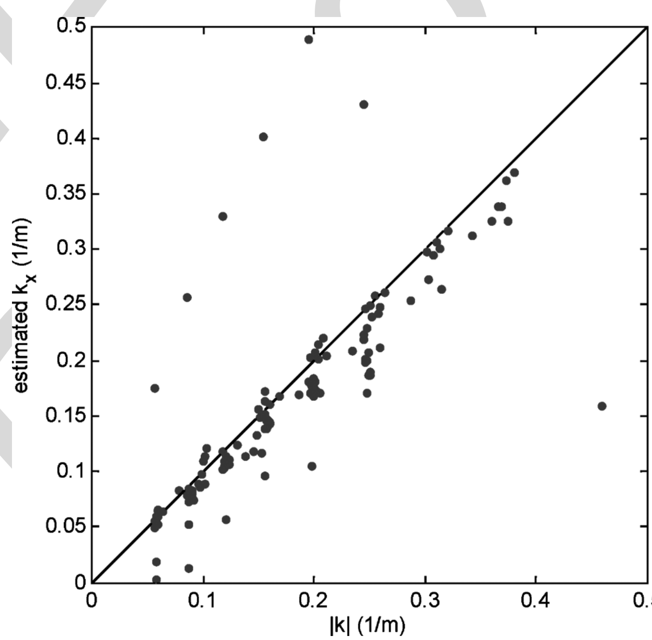

Fig. 9. Comparison of estimated and "true" wavenumbers [correlation coefficient $= 1.05$ and skill$(r^2) = 0.96$]. Data represent all analyzed frequencies and all locations in the tomographic domain.

C. *Applications in 2-D*

The wavenumber estimation methods based on fitting the cross-spectral correlation can be extended to a 2-D domain. This allows the wave direction to be included as an unknown parameter. Drawbacks of such an extension are given as follows: 1) the number of unknown variables is doubled (and this quadruples the computational effort for the wavenumber estimation procedure) and 2) the dimension of the cross-spectral correlation matrix is approximately squared, increasing both computational effort as well as memory requirements for the data analysis procedure. For example, the 2-D pixel array in the field data application included 1124 sample locations, yielding 632 250 useful cross-spectral correlation elements, each with a real and an imaginary component, at each of the six sample

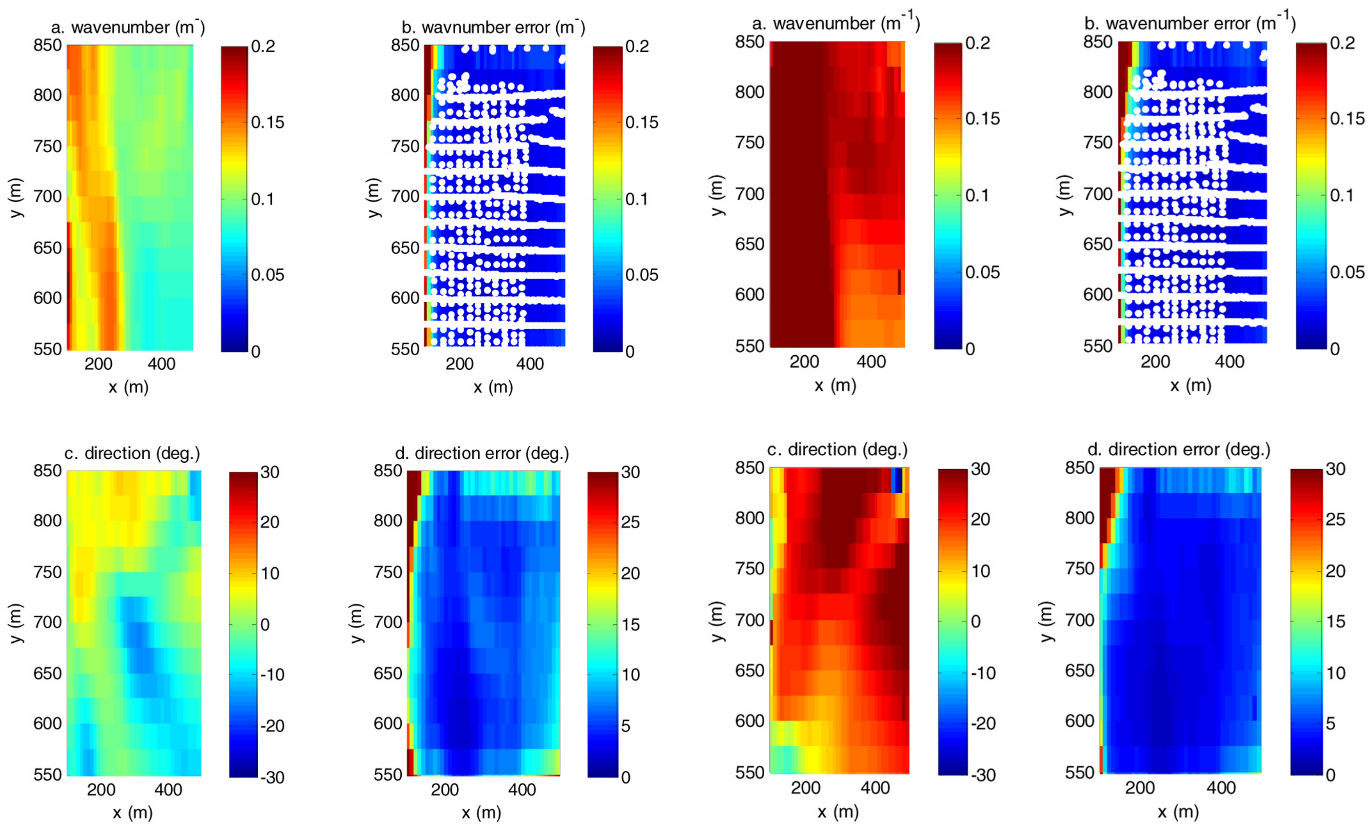

(a) (b)

AQ6 Fig. 10. (a) Estimates of (a) wavenumber magnitude and (c) wave direction and (b, d) predicted errors at a frequency of 0.10 Hz (10-s wave period). The median direction at the seaward boundary was $-5°$ (waves approach from the south, but nearly shore normal). White dots on the wavenumber error prediction plot indicate image pixel sample locations. (b) Estimates of wavenumber magnitude and wave direction and predicted errors at a frequency of 0.167 Hz (6-s wave period). The median direction at the seaward boundary was $+29°$ (waves from the north).

4/C

frequencies. The result is 7.5 million data values. It should be noted that the spatial extent of this sampling array is not unusually large, as it spans only a few hundred meters alongshore. Many useful applications could extend at least several to tens of kilometers alongshore. To overcome the data management hurdles, we solve the inverse problem locally over spatial regions where we assume the wavenumber and direction to be slowly varying. That is, we solve the problem at one spatial location at a time (i.e., with $M = 1$) rather than solving for wavenumbers at all locations simultaneously. Then, we move the analysis to each element of the tomographic domain. The revised approach still benefits from resolving both the frequency and spatial dependence of the cross-spectral correlation without having to assume a locally homogeneous bathymetry.

Fig. 10(a) and (b) shows the analysis of a 2-D domain. The results are plotted for two different frequencies (0.10 and 0.167 Hz). Fig. 10(a) (0.10 Hz) shows that the wavenumber is robustly estimated in much of the domain, indicated by error predictions that are much smaller than the minimum wavenumber. Errors are larger along the shoreline near $x = 100$ m. At the offshore boundary, the direction of wave approach varies somewhat but is generally close to shore normal. The median direction along the offshore boundary was $-5°$ (waves approaching slightly from the south); the median direction over the whole domain was $-1°$; and the median directional uncertainty was $7°$. Fig. 10(b) (0.167 Hz) shows that wavenumber is, again, robustly estimated. At the offshore boundary, the direction of wave approach was clearly from the north. The median direction along the offshore boundary was 28° (waves approach from the north); the median direction overall was 20°; and the median directional uncertainty was 4°. Fig. 11 shows independent estimates of the frequency- and direction-resolved spectrum obtained from an array of pressure sensors located 900 m offshore at a water depth of 8 m [33]. It shows the same differences in approach directions for the two frequencies presented in Fig. 10(a) and (b). For both frequencies, the directions estimated from the pressure sensors have larger magnitudes than the image-derived directions. This is consistent with effects of refraction over the 400-m propagation distance between the gage and the seaward boundary of our estimation domain. Correcting for refraction (symbols plotted in Fig. 11) significantly improves the comparison between the image- and pressure-based wave direction estimates.

D. Application to Bathymetry Inversion

While the wavenumber estimates are directly useful for characterizing the wave directional distribution and for testing wave dispersion relationships, a key motivation for this effort is to facilitate robust remote-sensing-based bathymetry estimation. Bathymetry estimation requires a solution of yet another inverse

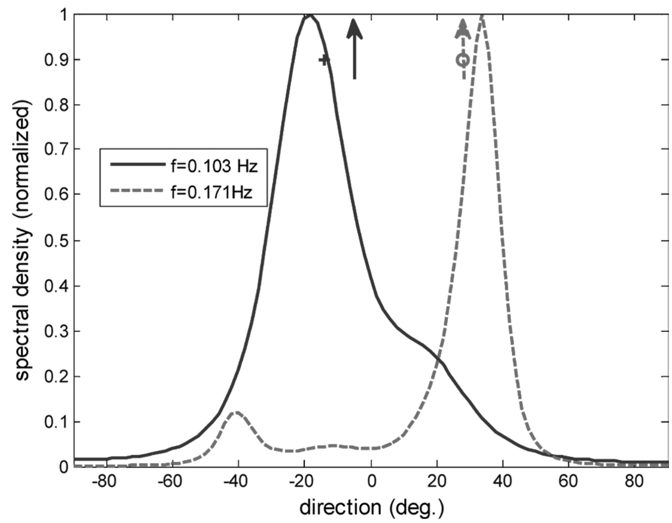

Fig. 11. Slices from directional wave spectrum based on *in situ* measurements at a water depth of 8 m. The two frequencies closest to 0.1 and 0.167 Hz were selected. Peak directions were -18 (0.1 Hz) and 34° (0.17 Hz). The refracted peak directions were computed for shoaling from a depth of 8 m to a depth of 5 m and are shown with symbols (+ for 0.1 Hz and ○ for 0.167 Hz). The arrows indicate the median direction at the offshore boundary corresponding to the 2-D wavenumbers of the motion imagery analysis.

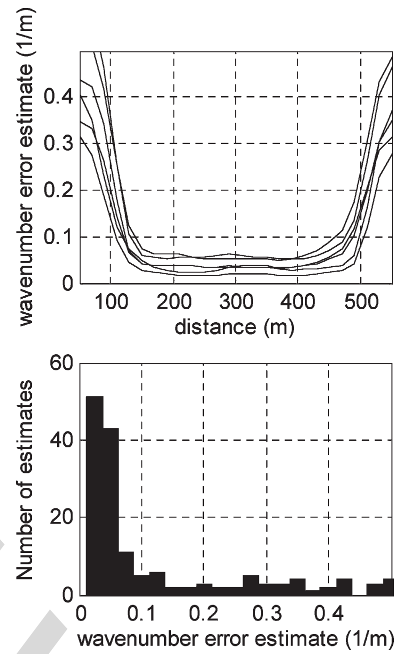

Fig. 12. Wavenumber error predictions and histogram.

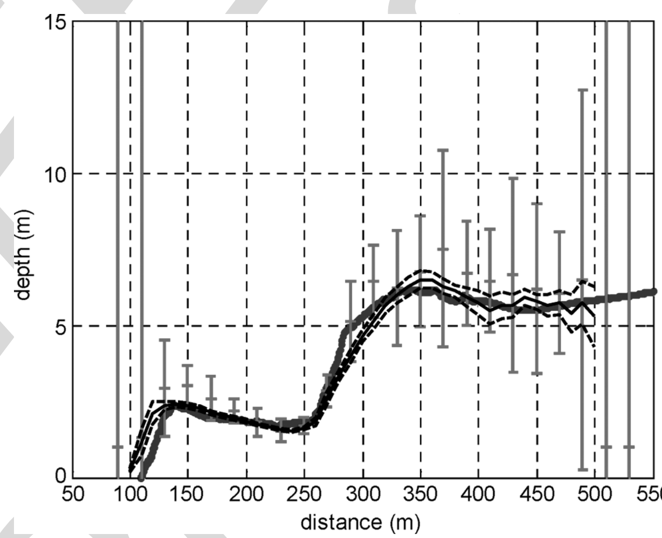

Fig. 13. Water depth estimated from image-derived wavenumbers. The estimates from the 1-D wavenumber inversion are shown with error bars and the estimates from the 2-D analysis are shown as a solid line with dashed lines, indicating one standard deviation error. The nearest survey observations are shown as blue dots.

problem using a dispersion model that relates wavenumber to water depth. We use linear wave theory, i.e.,

$$(2\pi f)^2 = gk\,\tanh(kh) \rightarrow k = \text{funct.}(f, h) \qquad (14)$$

where g is the gravitational acceleration, and h is the local water depth. Given values for f (i.e., sample frequencies) and h (a guess at the correct depth), this equation can be solved for wavenumbers (it is a transcendental equation, solved iteratively). We use the LM method to solve for the value of h that minimizes the error between the wavenumber predicted by (14) and that estimated from the imagery via (9). The advantage of separating the bathymetry inversion from the wavenumber inversion is that the quality of the image data can be objectively evaluated. Data with large errors can be rejected outright, or the errors can be used as weights in the inversion scheme, just as the coherence was used in (8). Furthermore, since each frequency is independent of the others, the depth inversion applied at each spatial location uses a number of independent wavenumber estimates. This should result in quantitatively accurate bathymetric error predictions, because the number of degrees of sampling freedom will not be overestimated. Otherwise, cross-spectral correlation estimates are not independent because data from each pixel are utilized multiple times as they is compared to itself and all the other pixels. Another reason for separating the wavenumber estimation from the bathymetry estimation is that the sensitivity of wavenumber to depth is very high in shallow water and is zero offshore. The near-zero sensitivity at the offshore region will destabilize a global bathymetry inversion, whereas this does not affect the wavenumber estimation problem.

The wavenumber error predictions obtained from the nonlinear inversion can be used to identify thresholds used to reject or weight the wavenumber estimates when applied to the depth inversion problem. Fig. 12 shows the spatial distribution of the errors and the error histogram from all the locations and frequencies. There appears to be a minimum error of approximately 0.05 m^{-1}. Thus, errors that are much larger than this value indicate relatively low-quality data. Using a Gibb's energy analogy [27], weights applied to the depth inversion were computed as $E = \exp(-\varepsilon/\kappa)$, where κ was 0.02 m^{-1}, and ε is the error prediction (as long as $\kappa < 0.1$, the choice of κ was not too important). The weight E is largest for error predictions approaching the minimum error, and E is small for larger errors.

Fig. 13 shows the resulting water depth estimates based on the 1-D (cross-shore) estimates of the wavenumber. Skillful depth estimates are obtained from depths between 2 and 6 m.

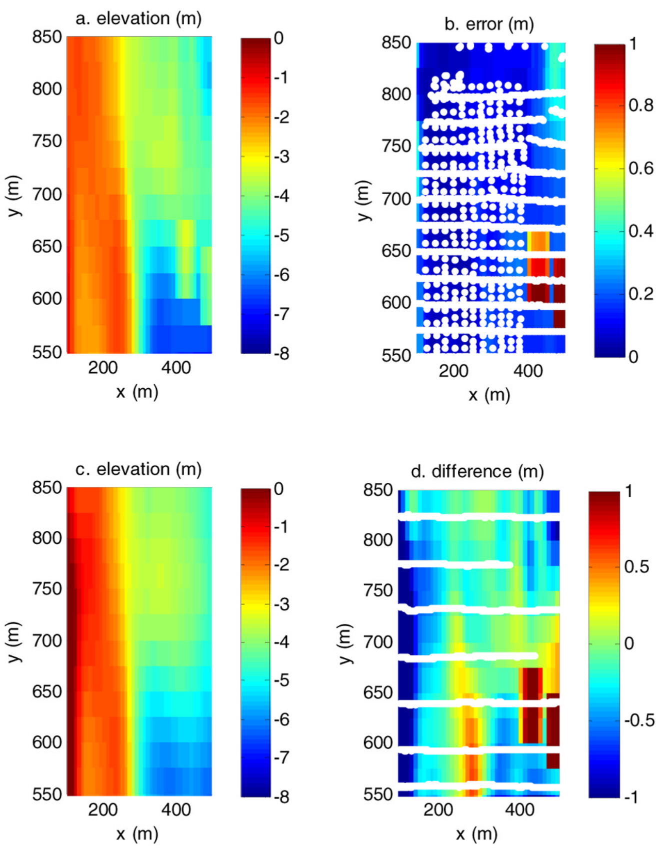

Fig. 14. Comparison of bathymetry derived using (a) 2-D wavenumber estimates and (c) surveyed (and spatially interpolated) bathymetry. Maps show (b) the predicted errors from the wavenumber inversion and (d) the actual differences between wavenumber inversion and survey. White dots on the error maps indicate the sample locations for both (b) imagery and (d) survey data sets.

4/C

The prediction is most accurate over the sandbar, where the mismatch between surveyed and estimated bathymetry is less than 10 cm, and the predicted errors are also small. Seaward of about 300 m (depths > 5 m), the bathymetry estimate is less accurate, and the error predictions are larger. Near the shoreline, the wavelength is short and poorly resolved; wavenumber error predictions are large, and the bathymetry estimate is poor.

The differences between the predicted and true bathymetries are not random. Offshore, the predictions are too deep. This is likely due to neglecting the wave direction for the 1-D analysis and interpreting the cross-shore wavenumber component as the wavenumber magnitude that appears in (14). In essence, the cross-shore wavenumber is too small, and the depth is overestimated. Near the shore, the bathymetry predictions are, again, too deep. This could result from neglecting the alongshore component of wavenumber, or it could be due to wave nonlinearity wherein waves travel faster than predicted by linear dispersion, and the resulting wavenumbers are smaller than expected. The offshore wave height of 0.5 m at the time of the analysis would lead to wave breaking at a water depth of roughly 1 m; hence, there was very little breaking over the bar—as evident in Fig. 4. Other mechanisms for causing discrepancies, such as setup or strong wave–current interactions are not likely to be too important because of the lack of wave breaking to force them.

Using the wavenumbers from the 2-D analysis to estimate the bathymetry (Figs. 13 and 14) results in shallower (and mostly improved) bathymetry both offshore and at the shallower portions of the profile, suggesting that refraction was, indeed, largely responsible for the discrepancies observed in the 1-D analysis. Larger errors in the middle of the 2-D region appeared where there was strong alongshore bathymetric variability (Fig. 4). This variability was not allowed by the smoothing properties inherent in the 2-D analysis approach.

IV. Discussion

A. *Comparison to Other Methods*

The proposed tomographic approach utilizing cross-spectral correlations from coastal imagery resolves spatial and frequency variability of the wavenumber field and includes error estimates that can be used to appropriately weight the wavenumber estimates. The proposed approach comes with a larger computational effort than other formulations. Is it worth the effort? The formulations given in (1)–(9) show that the theoretical underpinnings of all of the coherence-based wavenumber estimation approaches are equivalent. Therefore, applying each method to the 1-D test example should yield similar results. Differences between methods will result from the way that each approach rejects observation noise through smoothing at the expense of spatial, frequency, or direction resolution. Since we do not know the "true" answer (except through forward modeling from the surveyed bathymetry), this analysis will not necessarily identify the approach that is most accurate.

1) Time Delay Approach: We use the method described in [26] to filter the cross correlation (3) to estimate the time delays between different sample locations. Fig. 15 shows the resulting time delays between all sample pairs and the correlation at each delay. Immediately apparent is the rapid decorrelation with spatial separation. Nonetheless, time lag estimates are accurate compared to "true" values derived using the known wave speed via (2). The advantage of the time delay approach is that the phase ambiguity problem is minimized. This is particularly true in natural systems where the generally broad-band random waves will guarantee that a single time delay will maximize the correlation between sensors. (In laboratory settings with monochromatic waves, strong correlations can be found at lags that are multiples of the wave period.) Fig. 15 shows the phase ambiguity appearing for time lags exceeding 20 s (or about three cycles of the dominant 6-s wave period). A problem with the time delay approach is that it is not clear how the quality of the time delay estimates based on the correlation, which is exceeding low at many relevant lags, is identified. Nonetheless, we computed the wavenumber via an inverse solution of (2). [Inverse solutions of (2) are, in principle, linear and do not require iterations.] Fig. 16 shows wavenumber estimates based on the time delays. In the middle of the computational domain, the results are more or less equivalent to those in Fig. 8 at $f = 0.167$ Hz.

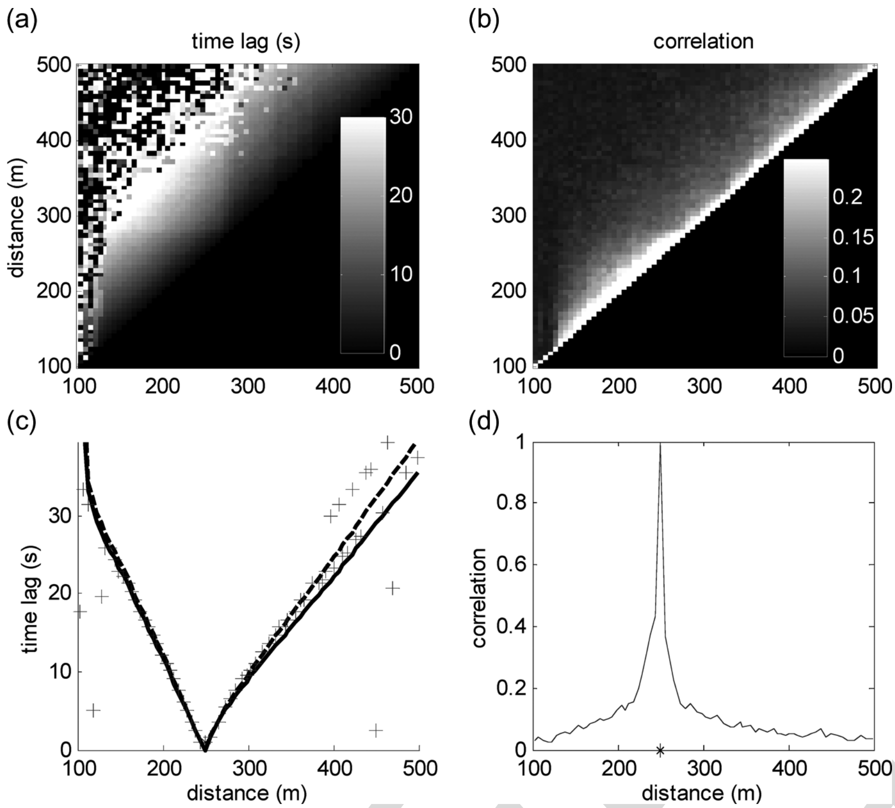

Fig. 15. (a and c) Time lag estimates and (b and d) associated correlation for all sensor pairs (top row) and for a slice comparing all sample locations to the location $x = 250$ m. The dashed line is the predicted time lag using the full dispersion equation at $f = 0.167$ Hz, and the solid line is the nondispersive shallow-water approximation.

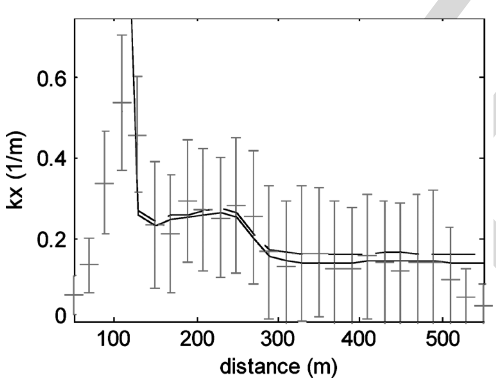

Fig. 16. Wavenumber estimate (and rms error prediction) using time lag data (assuming $f = 0.167$ Hz) compared to the linear wave theory prediction. The solid line is the theoretical prediction for nondispersive waves, and the dashed line is theoretical prediction for dispersive waves.

Another problem with the time delay approach is that comparisons to predictions from a wave dispersion equation (or its inverse) require specification of a dominant wave period. In the cross-spectral correlation methods, wave period (or frequency) is an independent variable, not a required input variable. The dependence of time delays for different wave periods shows that there could be considerable time delay dependence on wave period (dashed line in Fig. 15), and that these errors accumulate at large spatial lags.

2) Single-Mode (EOF) Approach: Given that the proposed nonlinear estimation routine worked well in the test case, we suspect that, due to the long time series and high coherence at several frequencies, the single-mode EOF approach would also be effective. Fig. 17 shows the results of that approach. The results are very good, with a few exceptions. There is clearly more short-scale variability in the EOF estimate, which did not include any smoothness constraint. Simple spatial filtering would achieve a smoother result. However, the EOF wavenumber estimate is clearly unstable in a few locations at frequencies with relatively low coherence. Unfortunately, there is not a clear method to identify the errors. There is no reason to restrict the EOF analysis to a single frequency, and therefore, consistency of estimates across a few frequencies may be used to provide improved uncertainty estimates, particularly if the results are used for bathymetry inversion. Furthermore, if there are multiple dominant wave trains at a single frequency, the EOF method could be applied to separate them as a preprocessing step to the nonlinear estimation approach.

B. Spatial Resolution

It is important to identify the spatial resolution of the wavenumber estimator presented in this analysis. Nearshore, spatial variations in the incident wavenumber (i.e., k_{wave}) result from corresponding variations in the bathymetry. The scale of the bathymetric variations might be shorter or longer than the wave scale, and they might be shorter or longer than what can be resolved by the sampling scheme.Intuitively, it seems reasonable that we can resolve bathymetric variations that are much longer than the incident wavelength. Can we resolve bathymetric variations that are shorter than the incident wavelength? How well must we resolve the incident waves? AQ7

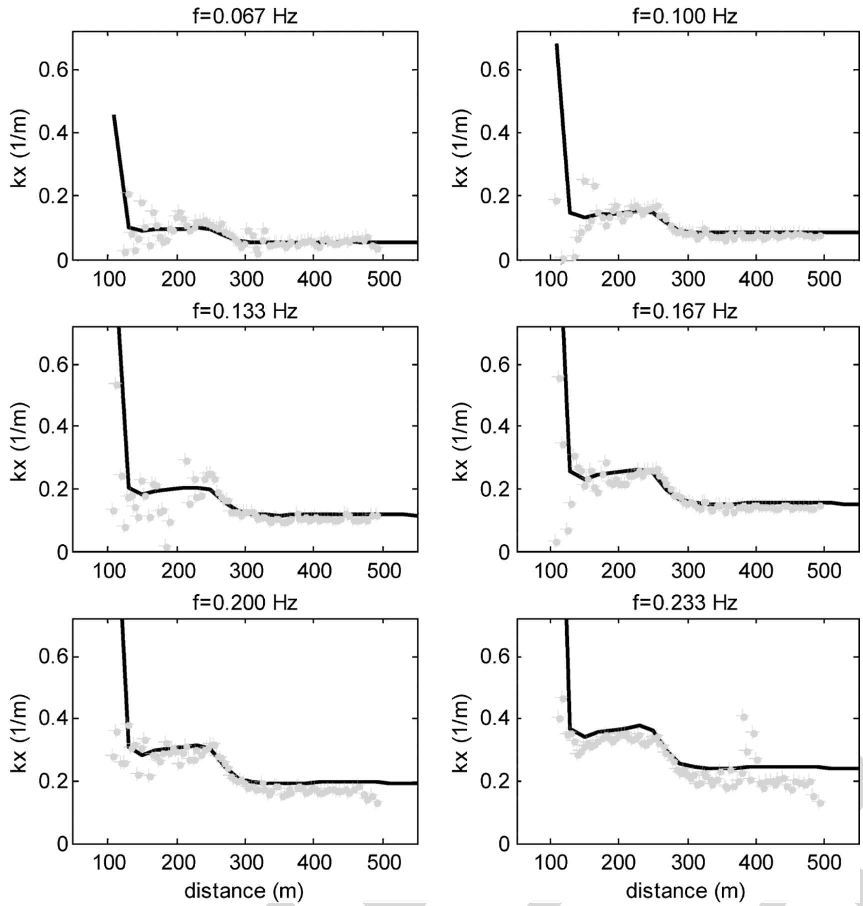

Fig. 17. Comparison of wavenumber estimates using the singular value method (+) to the linear wave theory prediction at each sample frequency (solid line).

To illustrate this problem, consider a flat seabed to which small sinusoidal bathymetric perturbations are added. The flat bottom yields a constant incident wave wavenumber k_{wave}. If the bathymetric perturbations are small, then the wavenumber is modulated as $k(x) = k_{\mathrm{wave}}(1 + \beta \cos[2\pi x k_{\mathrm{bathy}}])$, where k_{bathy} is the wavenumber of the bathymetric perturbation, β is the resulting (small) amplitude of that perturbation relative to the undisturbed wavenumber. Inserting a modulated wavenumber into the equation for the cross-spectral correlation (5) yields (e.g., the imaginary component)

$$\begin{aligned}\Im[C] &= \sin\left(2\pi\Delta x k_{\mathrm{wave}}\left\{1 + \beta \cos[2\pi\Delta x k_{\mathrm{bathy}}]\right\}\right)\\ &= \sin(2\pi\Delta x k_{\mathrm{wave}})\\ &\quad + \frac{\beta k_{\mathrm{wave}}}{2k_{\mathrm{bathy}}}\sin\left(2\pi\Delta x[k_{\mathrm{wave}} + k_{\mathrm{bathy}}]\right)\\ &\quad - \frac{\beta k_{\mathrm{wave}}}{2k_{\mathrm{bathy}}}\sin\left(2\pi\Delta x[k_{\mathrm{wave}} - k_{\mathrm{bathy}}]\right)\\ &\quad + o(\beta^2). \end{aligned} \tag{15}$$

The interaction of the incident wave signal and the bathymetric signal produces two scales of variability (as a function of spatial lag Δx) in addition to the wave scale. There is a longer scale response associated with the difference between the incident and bathymetric wavenumbers and a shorter scale response associated with their sum. The response of these contributions is linearly damped as k_{bathy} increases relative to k_{wave}.

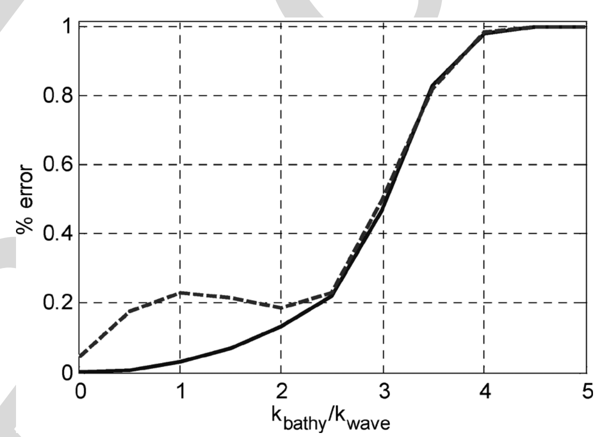

Fig. 18. Sensitivity of wavenumber estimation errors to bathymetric perturbation length scales k_{bathy}, normalized by the surface wavenumber k_{wave}. The two lines show the sensitivity for the case of no measurement noise (solid) and 10% noise (dashed). Other parameters were $k_{\mathrm{wave}} = 2\pi/25\ \mathrm{m}^{-1}$, $\Delta x = \Delta x_m = 2.5$ m, and $L_x = 5$m.

This simple example indicates that there are several factors that affect the ability to resolve short-scale bathymetric features. First, these features modulate the cross-spectral correlation most strongly when they are long compared to the incident wavelength (i.e., small values of $k_{\mathrm{bathy}}/k_{\mathrm{wave}}$). In practice, there is an additional damping of short features due to the spatial filtering that is imposed by our analysis. Fig. 18 shows the percent error associated with attempts to retrieve sinusoidal perturbations of the incident wavenumber. Synthetic cross-spectral correlation samples were generated from perturbed wavenumber profiles. In the second example, 10% percent noise was added to the "true" perturbed wavenumber profile. In the case without noise (Fig. 18, solid line), the retrieval errors are less than 20% for $k_{\rm bathy}/k_{\rm wave} < 2.5$. The error climbs rapidly for higher bathymetric wavenumbers due to the smoothing filter that completely removes features with a scale equal to the Nyquist wavenumber ($k_{\rm Nyq} = \pi/\Delta x_m$ or $k_{\rm Nyq}/k_{\rm wave} = 5$).

In the more realistic scenario where 10% percent noise was added to the observations (Fig. 18, dashed line), the error sensitivity is different. There is a local peak in the retrieval error at $k_{\rm bathy}/k_{\rm wave} = 1$. This occurs because the difference wavenumber term in (15) is zero, and only the sum wavenumber contributes to the signal. The sum wavenumber (shorter wavelength) is not well resolved by the sample spacing, and consequently, the perturbation is not well estimated. As $k_{\rm bathy}$ increases, the retrieval error slightly decreases because the difference wavenumber term, which is well resolved, once again contributes to the signal. Finally, further increases in $k_{\rm bathy}$ are not resolved as the smoothing filter again dominates the error.

There is a fortuitous relationship between sampling resolution capabilities and typical estimation requirements. Shorter scale bathymetric features are found in the shallowest waters where waves are most sensitive to depth variations. Since shore-based imaging typically has higher resolution closer to the shoreline, the short wavelength signals of interest are most likely to be resolved. In deep water, the length scales of bathymetric features are longer; the wavelengths that are sensitive to depth variations are also longer; and these longer scales still ought to be resolved by the shore-based sensor. As a rule-of-thumb (assuming measurement noise is unavoidable), the shortest (cross-shore dimension) resolved bathymetric feature will be about twice the wavelength of the incident waves that are resolved by the imaging system. Allowing that nearshore waves are inherently depth dispersive, which implies that $k_{\rm wave}h \leq 1$, this suggests that bathymetric features must be longer than about ten times the water depth. For average water depths of several meters, features that are tens of meters long are, in principle, resolvable. This resolution is about ten times better than what is achievable with the energy density identification approach [15], even with a similar pixel resolution (1–2 m), mainly because the assumption of a locally homogeneous bathymetry over the sampling array region is not required in the proposed method. The tradeoff is that the present approach only resolves a single dominant wavenumber, while the energy density approach resolves many different wavenumbers. The latter approach may perform better in the case of a directionally bimodal or very directionally broad-banded incident wave spectrum where the assumption of a single dominant wavenumber may be overly simplistic.

V. Conclusion

We have reviewed several approaches that have been used to estimate ocean surface gravity wavenumbers from wave-resolving image sequences. Two fundamentally different approaches exist that utilize this type of data. A power spectral density approach identifies wavenumbers that maximize image intensity variance. Alternatively, a cross-spectral correlation approach identifies wavenumbers that maximize intensity coherence. The first method finds, at an arbitrary wavenumber, the frequency associated with maximum spectral density. This approach requires application of a 2- or 3-D FFT to, typically, full frame images. The spatial resolution of the wavenumber estimates is typically $O(100)$ times the image pixel resolution.

The second approach finds, at each resolved frequency, the wavenumber that maximizes the observed cross-spectral coherence. Numerous solution methods have been suggested for this approach, including cross correlation and empirical orthogonal function analysis. Here, we developed a solution based on a tomographic analysis that utilizes a nonlinear inverse method and may be applied to both time- and frequency-domain analyses. We demonstrate that a formal treatment of the problem leads to a nonlinear inverse problem that can be solved to yield robust wavenumber estimates and error predictions.

We expand in detail a frequency-domain solution approach that yields robust retrievals of wavenumber estimates from the imagery. The approach is tolerant to noise and other forms of sampling deficiency and can be applied to arbitrary sample patterns, as well as to full frame imagery. The approach provides error predictions that are useful for quality control and subsequent applications to, for instance, bathymetry estimation. A quantitative analysis of the resolution of the method indicates that the cross-spectral correlation fitting approach has about ten times better resolution than the power spectral density fitting approach. Furthermore, the resolution analysis provides a rule of thumb for bathymetry estimation: Cross-shore spatial patterns may be resolved if their length is ten times the water depth. This guidance can be applied to sample design to include constraints on both the sensor array (image resolution) and the analysis array (tomographic resolution). Finally, the method supports bathymetry estimation through inversion of a wave dispersion model. It does this by providing robust statistically consistent and independent wavenumber estimates at multiple wave frequencies.

Acknowledgment

The authors would like to thank the Beach Wizards who contributed to the development of this effort. The authors are particularly indebted to P. Catalan for the encouragement, evaluation, and critical review. Comments from an anonymous reviewer considerably improved the clarity of the manuscript. Finally, we could not have performed a sensible field evaluation without the stage set by both the Army Corps of Engineers' FRF and R. Holman's Argus program.

References

[1] R. A. Holman and J. Stanley, "The history and technical capabilities of Argus," *Coast. Eng.*, vol. 54, no. 6/7, pp. 477–491, Jun./Jul 2007.

[2] S. G. J. Aarninkhof and R. A. Holman, "Monitoring the nearshore with video," *Backscatter*, vol. 10, no. 2, pp. 8–11, 1999.

[3] H. F. Stockdon and R. A. Holman, "Estimation of wave phase speed and nearshore bathymetry from video imagery," *J. Geophys. Res.—Oceans*, vol. 105, no. C9, pp. 22 015–22 033, Sep. 15, 2000.

[4] K. T. Holland, "Application of the linear dispersion relation with respect to depth inversion and remotely sensed imagery," *IEEE Trans. Geosci. Remote Sens.*, vol. 39, no. 9, pp. 2060–2072, Sep. 2001.

[5] T. C. Lippmann and R. A. Holman, "Quantification of sand bar morphology: A video technique based on wave dissipation," *J. Geophys. Res.*, vol. 94, no. C1, pp. 995–1011, 1989.

[6] S. G. J. Aarninkhof, B. G. Ruessink, and J. A. Roelvink, "Nearshore subtidal bathymetry from time-exposure video images," *J. Geophys. Res.*, vol. 110, no. C6, p. C06 011, 2005. DOI:10.1029/2004JC002791.

[7] S. G. J. Aarninkhof and B. G. Ruessink, "Video observations and model predictions of depth-induced wave dissipation," *IEEE Trans. Geosci. Remote Sens.*, vol. 42, no. 11, pp. 2612–2622, Nov. 2004.

[8] N. G. Plant and R. A. Holman, "Intertidal beach profile estimation using video images," *Mar. Geol.*, vol. 140, no. 1, pp. 1–24, Jul. 1997.

[9] S. G. J. Aarninkhof, I. L. Turner, T. D. T. Dronkers, M. Caljouw, and L. Nipius, "A video-based technique for mapping intertidal beach bathymetry," *Coast. Eng.*, vol. 49, no. 4, pp. 275–289, Oct. 2003.

[10] S. M. Adler-Golden, P. K. Acharya, A. Berk, M. W. Matthew, and D. Gorodetzky, "Remote bathymetry of the littoral zone from AVIRIS, LASH, and QuickBird imagery," *IEEE Trans. Geosci. Remote Sens.*, vol. 43, no. 2, pp. 337–347, Feb. 2005.

[11] D. R. Lyzenga, N. P. Malinas, and F. J. Tanis, "Multispectral bathymetry using a simple physically based algorithm," *IEEE Trans. Geosci. Remote Sens.*, vol. 44, no. 8, pp. 2251–2259, Aug. 2006.

[12] J. V. Toporkov, D. Perkovic, G. Farquharson, M. A. Sletten, and S. J. Frasier, "Sea surface velocity vector retrieval using dual-beam interferometry: First demonstration," *IEEE Trans. Geosci. Remote Sens.*, vol. 43, no. 11, pp. 2494–2502, Nov. 2005.

[13] J. P. Dugan, C. C. Piotrowski, and J. Z. Williams, "Water depth and surface current retrievals from airborne optical measurements of surface gravity wave dispersion," *J. Geophys. Res.*, vol. 106, no. C8, pp. 16 903–16 915, 2001.

[14] J. P. Dugan, H. H. Suzukawa, C. P. Forsyth, and M. S. Farber, "Ocean wave dispersion surface measured with airborne IR imaging system," *IEEE Trans. Geosci. Remote Sens.*, vol. 34, no. 5, pp. 1282–1284, Sep. 1996.

[15] C. C. Piotrowski and J. P. Dugan, "Accuracy of bathymetry and current retrievals from airborne optical time-series imaging of shoaling waves," *IEEE Trans. Geosci. Remote Sens.*, vol. 40, no. 12, pp. 2606–2618, Dec. 2002.

[16] T. C. Lippmann and R. A. Holman, "Phase speed and angle of breaking waves measured with video techniques," in *Coastal Sediments '91*, N. Kraus, Ed. New York: ASCE, 1991, pp. 542–556.

[17] K. T. Holland, J. A. Puleo, and T. N. Kooney, "Quantification of swash flows using video-based particle image velocimetry," *Coast. Eng.*, vol. 44, no. 2, pp. 65–77, Dec. 2001.

[18] P. S. Bell, "Shallow water bathymetry derived from an analysis of X-band marine radar images of waves," *Coast. Eng.*, vol. 37, no. 3/4, pp. 513–527, Aug. 1999.

[19] J. A. Puleo, G. Farquharson, S. J. Frasier, and K. T. Holland, "Comparison of optical and radar measurements of surf and swash zone velocity fields," *J. Geophys. Res.*, vol. 108, no. C3, p. 3100, 2003. DOI:10.1029/2002JC001483.

[20] P. A. Catálan and M. C. Haller, "Remote sensing of breaking wave phase speeds with application to non-linear depth inversions," *Coast. Eng.*, vol. 55, no. 1, pp. 93–111, Jan. 2008.

[21] B. Jahne, J. Klinke, and S. Waas, "Imaging of short ocean wind waves: A critical theoretical review," *J. Opt. Soc. Amer. A, Opt. Image Sci.*, vol. 11, no. 8, pp. 2197–2209, Aug. 1994.

[22] C. M. Senet, J. Seemann, and F. Ziemer, "The near-surface current velocity determined from image sequences of the sea surface," *IEEE Trans. Geosci. Remote Sens.*, vol. 39, no. 3, pp. 492–505, Mar. 2001.

[23] C. G. Gelpi, B. C. Schuraytz, and M. E. Husman, "Ocean wave height spectra computed from high-altitude, optical, infrared images," *J. Geophys. Res.*, vol. 106, no. C12, pp. 31 403–31 413, 2001.

[24] W. Menke, *Geophysical Data Analysis: Discrete Inverse Theory*. New York: Academic, 1989.

[25] W. Munk, P. Worcester, and C. Wunsch, *Ocean Acoustic Tomography*. Cambridge, U.K.: Cambridge Univ. Press, 1995.

[26] S. Takashima, H. Asanuma, and H. Niitsuma, "A water flowmeter using dual fiber Bragg grating sensors and cross-correlation technique," *Sens. Actuators A, Phys.*, vol. 116, no. 1, pp. 66–74, 2004.

[27] S. Stramaglia, A. Refice, and L. Guerriero, "Statistical mechanics approach to the phase unwrapping problem," *Phys. A*, vol. 276, no. 3, pp. 521–534, Feb. 2000.

[28] T. H. C. Herbers, S. Elgar, and R. T. Guza, "Generation and propagation of infragravity waves," *J. Geophys. Res.*, vol. 100, no. C12, pp. 24 863–24 872, 1995.

[29] J. M. Oltman-Shay and R. T. Guza, "A data-adaptive ocean wave directional-spectrum estimator for pitch and roll type measurements," *J. Phys. Oceanogr.*, vol. 14, no. 11, pp. 1800–1810, Nov. 1984.

[30] M. A. Merrifield and R. T. Guza, "Detecting propagating signals with complex empirical orthogonal functions: A cautionary note," *J. Phys. Oceanogr.*, vol. 20, no. 10, pp. 1628–1633, Oct. 1990.

[31] W. H. Press, S. A. Teukolsky, W. T. Vetterling, and B. P. Flannery, *Numerical Recipes in C: The Art of Scientific Computing*, 2nd ed. Cambridge, U.K.: Cambridge Univ. Press, 1992.

[32] W. A. Birkemeier and C. Mason, "The CRAB: A unique nearshore surveying vehicle," *J. Surv. Eng.*, vol. 110, no. 1, pp. 1–7, 1984.

[33] C. E. Long and J. M. Oltman-Shay, "Directional characteristics of waves in shallow water," Coastal Eng. Res. Center, Field Res. Facility, U.S. Army Eng. Waterways Experiment Station, Vicksburg, MS, Tech. Rep. CERC-91, 1991.

Nathaniel G. Plant received the B.S. degree in earth sciences in 1989 and the M.S. degree in 1990 from the University of California, Santa Cruz, and the Ph.D. degree in oceanography from Oregon State University, Corvallis, in 1998.

He was an Oceanographer with the Naval Research Laboratory, Stennis Space Center, MS, from 2002 to 2007 and is currently an Oceanographer with the U.S. Geological Survey, St. Petersburg, FL. His research interests include studies of coastal processes and morphological evolution and prediction using both direct and remote sensing methods.

K. Todd Holland received the B.S. degree from Duke University, Durham, NC, in 1986 and the M.S. and Ph.D. degrees in oceanography from Oregon State University, Corvallis, in 1992 and 1995, respectively.

Since 1995, he has been an Oceanographer with the Naval Research Laboratory, Stennis Space Center, MS. He is a leading expert in the application of remote sensing technologies to the study of nearshore processes, particularly with respect to the use of motion imagery. He is currently developing new innovative techniques to characterize coastal areas using camera systems on small aerial vehicles.

Merrick C. Haller received the B.S. degree from Purdue University, West Lafayette, IN, in 1993, and the M.C.E. and Ph.D. degrees in civil engineering from the University of Delaware, Newark, in 1996 and 1999, respectively.

He currently holds joint appointments as an Assistant Professor in the School of Civil and Construction Engineering and the College of Oceanic and Atmospheric Sciences, Oregon State University, Corvallis. He has also worked as a Research Engineer with Veridian Systems Division and the University of Michigan, Ann Arbor. His present research interests include multisensor remote sensing of the nearshore ocean, wave breaking, rip currents, and wave–current interactions.

AUTHOR QUERIES

AUTHOR PLEASE ANSWER ALL QUERIES

ATTN: If you are paying to have all or some of your figures appear in color in the print issue, it is very important that you fill out and submit a copy of the IEEE Page Charge & Reprint Form along with your proof corrections. This form is available from the same URL where these page proofs were downloaded from. Thank you.

AQ1 = Rephrased. Edits correct?
AQ2 = Edits correct?
AQ3 = Ability of?
AQ4 = Lone left parenthesis was deleted. Original meaning preserved?
AQ5 = Added "respectively." Edits okay?
AQ6 = Several changes done. Original meaning preserved?
AQ7 = Please change figure labels to distinguish one from the other.

END OF ALL QUERIES